International Journal of Machine Tools & Manufacture 190 (2023) 104050

Contents lists available at ScienceDirect

International Journal of Machine Tools and Manufacture

journal homepage: www.elsevier.com/locate/ijmactool

Investigation of the grain deformation to orthogonal cutting process of the textured Alloy 718 fabricated by laser powder bed fusion

Lingshan Li [a,b], Hao Chen [a,**], Zhirong Liao [b,*], Yue Yang [b], Dragos Axinte [b]

[a] Department of Mechanical, Materials, and Manufacturing, University of Nottingham Ningbo China
[b] Department of Mechanical, Materials, and Manufacturing, University of Nottingham, UK

ARTICLE INFO

Handling Editor: Prof Dragos axinte

Keywords:
Laser powder bed fusion (LPBF)
High-strain-rate shear removal
Quasi-in-situ observation
Crystallographic texture
Deformation mechanism
Most active slip trace

ABSTRACT

In the laser powder bed fusion (LPBF), the grains grow in preferential directions depending on the scanning strategies, which results in layer-by-layer builds of particular crystallographic textures. The unique microstructure formed by LPBF results in anisotropic properties of the built structure at both macro and micro levels. To understand the grain deformation of the textured alloy fabricated by LPBF in the high-strain-rate shear process, Alloy 718 was used as an example in this work. Bulk samples with different metallurgical textures were deliberately fabricated by LPBF via three laser rotation angles, namely 0°, 67° and 90°, and then four thin slices obtained from bulks were subjected to "quasi-in-situ" grain deformation investigation through orthogonal cutting (a simple shear loading condition). The evolution of crystal orientations and morphologies, including size and shape, were traced before and after shear deformation. A full-field crystal plasticity simulation was used to quantify the stress status for grains obtained from EBSD data. This for the first time reveals the crystallographic level deformation history for hundreds of microns during a high strain rate shear removal deformation. Due to the carefully retained deformation history (i.e., typical bulges and slip bands) on the surface, a repeated deformation pattern was observed, attributing to the non-homogeneous deformation of typical build-directional blocks. The most active slip trace of deformed grain was calculated and verified based on the dominated slip bands within individual grains. The slip trace direction and intensity were quantified for different textured Alloy 718. Since the slipping-based deformation for an orientated grain is represented by its most active slip trace, a deformation tendency map is obtained by combining the shear direction, slip system and grain morphology. It reveals that grains in high texture intensity workpieces generally follow the macro shear-based deformation, while with the decrease in texture intensity, the plastic anisotropy is significant at the grain scale. Grains with similar orientations may also result in localised deformation anisotropy due to the different morphologies.

1. Introduction

Laser powder bed fusion (LPBF) is one of the additive manufacturing (AM) processes that offers a unique advantage for low-volume and high-geometrical complexity productions, owning to its track-by-track and layer-by-layer fabricating manner [1,2]. The intense energy inputs in LPBF generate melt pools with sharp thermal gradients (**G**) and high cooling rates (10^4~10^6 K/s), causing rapid solidification [3]. This leads to unique epitaxial grain growth along the build direction (BD) in various materials, such as nickel-based superalloys [4], aluminium alloys [5] and titanium alloys [6], which exhibit quite different microstructures compared with the conventional cast and wrought alloys [7,8]. This is because the grain growth direction is sensitive to the process parameters in the laser track and between layers. Among these parameters, the influential factors that dominate the resultant microstructure are laser power, layer thickness and, more importantly, scanning strategies (beam path, scanning speed, hatch spacing). It was reported that the microstructure could be controlled by scanning strategies [9], such as the degree-rotation between layers (e.g., 0°, 67° or 90° rotations) [10,11]. These scanning paths have a dominant effect on the grain growth pattern, resulting in different crystallographic textures and characteristic grain morphologies in as-built alloys.

As one of the target materials for additive manufacturing, Nickel-based superalloys (e.g., Alloy 718), have been widely used in

* Corresponding author.
** Corresponding author.
E-mail addresses: Hao.Chen@nottingham.edu.cn (H. Chen), liaozhironghit@hotmail.com (Z. Liao).

https://doi.org/10.1016/j.ijmachtools.2023.104050
Received 23 January 2023; Received in revised form 26 May 2023; Accepted 11 June 2023
Available online 17 June 2023

aerospace and nuclear industries due to their high-temperature stability [12]. In particular, the additively manufactured Alloy 718 exhibits anisotropic properties with unique crystallographic textures [13]. These textures may lead to preferred deformation pattern in a loading condition (e.g., tension, compression or shearing). Since scanning strategies change grain growth patterns by providing different thermal conditions, variable grain morphologies (size and shape) are formed in as-printed Alloy 718. Elongated grains with high aspect ratios is commonly observed in <001>//BD texture [14,15], where grains usually grow along the build-direction. In addition, the columnar grains are much easier to grow in the <011> direction in the 0° rotation scanning strategy. In the 67°-rotation scanning strategy, grain growth pattern is more randomised by alternating the scanning direction in each layer, suppressing elongated growth and varying grain orientations [16]. It was found experimentally that 90° and 67° specimens exhibited higher yield strength than that of 0°-built specimens [17]. Moreover, samples with stronger retained texture exhibited higher yield strength and lower elongation when compared with weaker-textured samples under the build-directional loading direction [18]. To estimate properties in such different textures composed of unique grain morphology, grain size may need to be assessed with its morphology instead of an average value.

Hitherto, LPBF technology has been successfully used to build Alloy 718 structures with different crystallographic textures. It is also recognised that the additively manufactured Alloy 718 components are often subjected to post-mechanical machining operations to achieve the required dimensional accuracy [19] and functional performances [20,21]. Understanding the response of the textured structure and grain morphology to mechanical machining is therefore critical to estimate the machinability of LPBF-fabricated alloy. It is reported the unique microstructure formed via a layer-by-layer fabrication manner can have a strong influence on structure-property relationship, such as tensile [22], creep and compression [23], for AM-ed alloys. And the complete characteristics at grain scale can be captured (e.g., tensile and compression test). Nevertheless, different from the tension or compression, in which the uniaxial loading is applied for the whole sample, the machining-induced deformation only occurs in a roughly 100-μm region close to the free surface. Therefore, plastic deformation is confined to a narrow region, where dramatic deformation often leads to grain refinement and orientation change [24]. Due to the difficulty of tracing grain evolution in such a narrow region [25], the deformation mechanism of the resultant crystallographic textures caused by the cutting process is still not well understood. Indeed SEM-based in-situ machining deformation has been investigated within several grains [26]. However, to the author's best knowledge, few attempts were reported to precisely trace the machining-induced deformation grain by grain in a high-strain-rate machining process. Since the shear process is conducted at the macro level, the deformation mechanism within several grains [27,28] have a limit on explaining the rule of texture-based deformation. This is attributed to the complexity of slip transfer across the grain boundaries and the uncertainty of stress loading at grain level [23]. It indicates that the texture-based deformation should be investigated based on statistical analysis at grain scale. The counted grains should be representative of the deformation caused by macro-cutting.

Therefore, in this work, a "quasi-in-situ" crystallographic investigation based on EBSD and SEM was performed on the textured Alloy 718 to trace the grain deformation during the orthogonal cutting process. The orthogonal cutting was employed to provide a clear shear-based deformation condition. Four unique textured Alloy 718 were carefully prepared and representative grains near the machined surface were traced to reveal the crystallographic deformation mechanism.

The uniqueness of this work is that the typical grains within the crystallographic texture of LPBF Alloy 718 can be identified before and after plastic deformation. This ensures the shear-based deformation mechanism can be unveiled via the evolution of grain orientation and morphology. The direction and intensity of the most active slip traces for the textured Alloy 718 samples were quantified based on the Taylor-based plasticity model. This is the first time in the literature to report the deformation of grains in textured LPBF-built structures (e.g. Alloy 718) responds to cutting process.

The as-built alloys usually exhibit different characteristic grains and unique textures, depending on the scanning strategies. These crystallographic characteristics significantly influence the shear-based deformation. It is recognised that the original grains near the machined surface (Fig. 1a) are hard to retain and trace due to the large sample dimension and serious plastic deformation in the cutting process. This impedes the precise experimental investigation of the machining-induced deformation associated with the evolution of grain morphologies and orientations. As a result, the deformation mechanism of as-built alloys with unique crystallographic textures in machining remains not fully revealed yet. To tackle this difficulty, the experimental methodology was carefully designed to retain the deformation history of representative grains in textured alloys. This allows the deformation mechanism to be characterised by detailing the changes of morphologies and orientations of exactly the same grains in the textured as-built alloys.

In this study, through a specific crystallographic tracing, we are able to figure the deformation of representative grains before and after cutting for hundreds of microns. It is conducted based on the typical bulges and slip bands on the observational surface (Fig. 1b), to reveal the specific grain deformation that depend on the LPBF induced crystallographic texture. The representative deformation features retained on the surface, especially for slip bands, allow us to reveal the relationship between oriented grains and shear-based deformation by the most active slip trace as Fig. 1c. Based on this, the slip trace direction and intensity of all representative grains were quantified, enabling the prediction of textured deformation through grain orientation and morphology. A full-field crystal plasticity simulation was used to quantify the stress status for grains obtained from EBSD data. This study will be useful for the additive manufacturing community to understand how textured material deforms during mechanical machining.

2. Experimental methods

2.1. Proposed concept

To study the effect of different textured Alloy 718 on shear-based deformation, three scanning strategies (0°, 67° and 90° rotation layer by layer) were used to fabricate crystallographic textured cubes as depicted in Fig. 2a–c. The 0° rotation strategy repeats the same scanning path to provide a stable thermal gradient conducive to grain growth along the build direction. 90° rotation strategy repeats every two layers and form strong cube textures while the 67° rotation strategy avoids repeating scanning directions, fabricating grains without preferred orientation. These three scanning strategies yield typical microstructures that are widely used in additive manufacturing field. Two samples (01T and 02T) were obtained from 0° rotation scanning strategy due to two different textures in the XZ and YZ planes. Only one sample was obtained from 90° (Fig. 2b) and 67° (Fig. 2c) rotation scanning strategies respectively since samples from XZ and YZ planes are equivalent in both scanning strategies. To compare the deformation of typical grains in the textured Alloy 718 before and after cutting, EBSD&SEM characterisation at the same zone near the machined surface was performed. It should be noted that the "quasi-in-situ" investigation was only conducted for the machining process instead of LPBF process. A "T-shape" label was marked on the carefully polished samples as a reference, allowing the same area to be detected under EBSD&SEM before and after cutting as shown in Fig. 2d. It must be emphasised that no polishing was conducted after the cutting experiment to retain the history of cutting on the grains. As such, the original grains, including morphologies, orientations and slip traces, can be analysed before cutting, as in Fig. 2e, and then be compared with grains after cutting as in Fig. 2f. The dtislocation density, grain boundary curving and orientation change were quantitatively

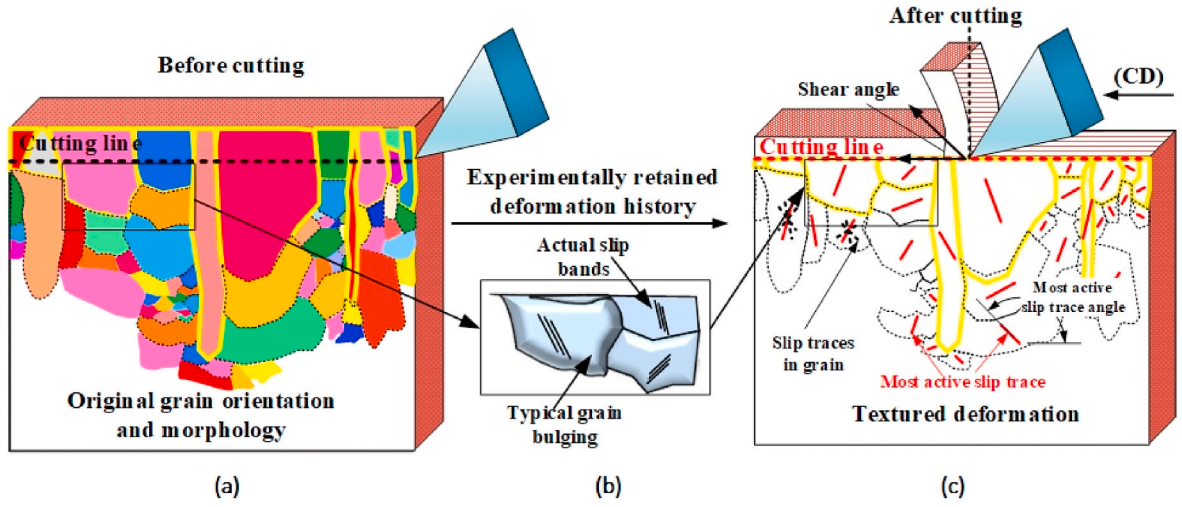

Fig. 1. Schematics of quasi-in-situ investigation of grain deformation in textured Alloy 718 fabricated by LPBF. (a) Original grain orientation and morphology in the LPBF-fabricated Alloy 718, (b) Experimentally retained deformation history, including slip bands and typical grain bulging, (c) The relationship between the cutting tool and grain slip system/morphology in the textured deformation.

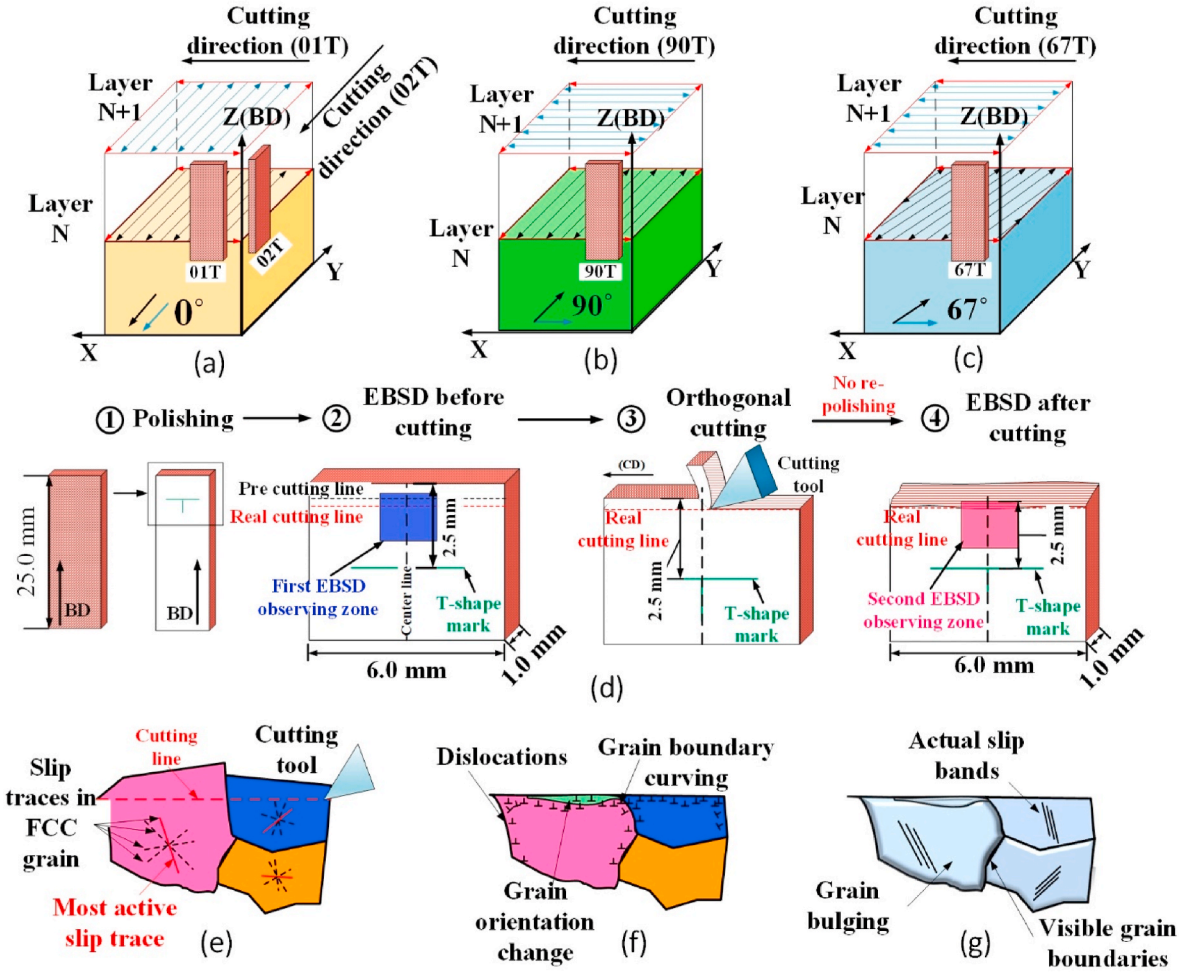

Fig. 2. Illustration of quasi-in-situ investigation of grain deformation in crystallographic textured Alloy 718. (a–c) Schematics of scanning strategies and cutting directions for four samples - see brown parallelepipeds - (01T, 02T, 90T and 67T) obtained from different LPBF built cubes; (d) Schematics of quasi-in-situ investigation processing, including polishing, first EBSD&SEM observation, orthogonal cutting and second observation; (e) Schematics of grains observed under EBSD before cutting (slip traces in FCC can be calculated based on IPF); (f) Schematics of grains observed under EBSD after cutting; (g) Schematics of grains observed under SEM after cutting (the slip bands and part of grain boundaries are visible due to deformation).

investigated. Furthermore, the slip bands and grain bulging can be found after cutting by combining EBSD and SEM results (Fig. 2g).

2.2. Preparation of as-built alloy 718 specimens

The gas atomised Alloy 718 powders (BLT Cop., China) with a particle size range of 15~45 μm (Fig. 3a) were used to fabricate specimens at a dimension of 35 mm × 25 mm × 25 mm (Fig. 3b). A BLT S200 printer with a 500 W Yb continuous fibre laser with a laser spot size of 60 μm was used for LPBF processing. The chamber was filled with 99.99% nitrogen to ensure the oxygen content was below 200 ppm. Three scanning strategies (Fig. 2a–c), 0°, 90 and 67°-rotation angles of the laser beam trajectory, were employed to deliberately generate different crystallographic textures. It is worth noting that these three scanning strategies are commonly employed in the commercial printing systems. Therefore, the investigation of their influence on machining-induced deformation can provide valuable insights. Other processing parameters such as laser power, scanning speed, hatch spacing, and

Table 1
Processing parameters for Alloy 718 fabrication with three scanning strategies to enable the generation of different crystallographic textures.

Specimen	Scanning strategies	Laser power (W)	Scanning speed (mm/s)	Hatch spacing (μm)	Layer thickness (μm)
01T 02T	0°-rotation	135	800	80	20
90T	90°-rotation				
67T	67°-rotation				

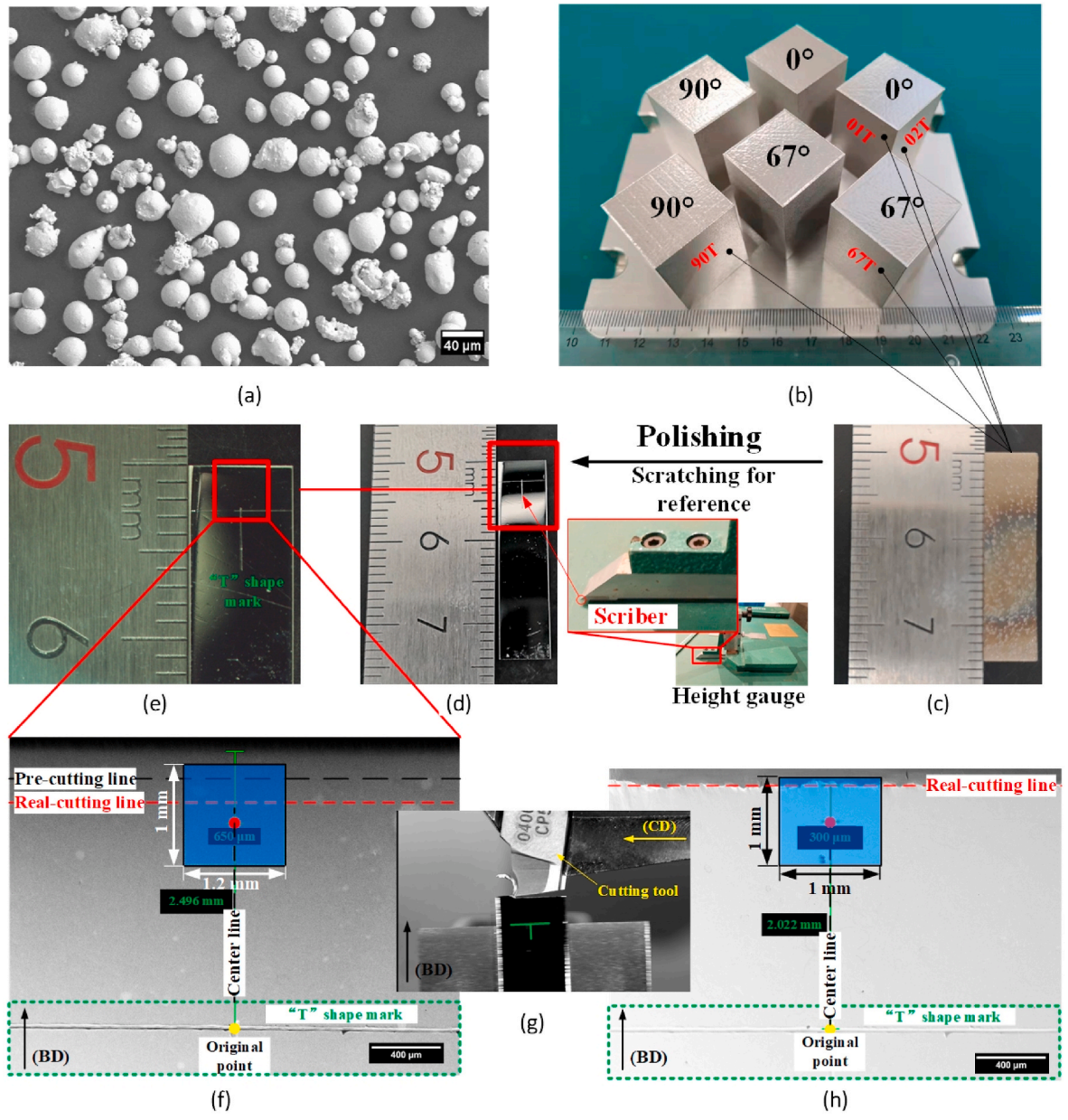

Fig. 3. Schematics of three scanning strategies and quasi-in-situ investigation processes. (a) Alloy 718 powder; (b) As-built cubes of 0°-rotation, 90°-rotation and 67° rotation scanning strategies; (c) Unpolished samples; (d) Polished samples; (e) "T" shape mark (scratched by scriber of height gauge) as the reference for observing the same zone before and after cutting; (f) and (h) are the corresponding zones localized by "T" shape scratch before and after cutting under the SEM and the blue rectangles are the zone for EBSD; (g) Processing of orthogonal cutting including cutting tool and cutting direction (CD).

layer thickness are selected to fabricate nearly defect-free parts [29] (porosity less than 0.05%) for cutting test in this work as shown in Table 1.

Four test workpieces with dimensions of 24 mm × 6 mm × 1 mm were obtained from as-built specimens by EDM as shown in Fig. 2b. In the three scanning strategies, XZ and YZ planes of 90° and 67° rotation strategies are equivalent due to the repeatedly rotated angles layer by layer, while XZ and YZ planes in the 0°-rotation strategy are dissimilar for their unidirectional scanning pattern. Therefore, two workpieces were obtained from the XZ and YZ planes from Fig. 2a, named 01T and 02T, respectively. It should be noted that the machining surfaces of 01T and 02T are the same surface (XY plane), but the cutting direction is perpendicular as shown in Fig. 2a. Workpieces of 90T and 67T were obtained from the XZ plane of specimens printed by 90° and 67°-rotation strategies respectively as shown in Fig. 3b and c. All cutting directions in this work are perpendicular to the build direction.

2.3. Quasi-in-situ observation of crystallographic texture and orthogonal cutting tests

The orthogonal cutting test was conducted by a customised Pendulum-based cutting test rig for small workpiece machining as detailed in Ref. [30] to provide a simple shear-based deformation condition. The cutting width, depth and speed were 1 mm, 0.2 mm and 112 m/min respectively, and a carbide cutting tool (SECO tools, LCGF160402-400-GG CP500) with a rake angle of 21° was used. The selected cutting depth of 0.2 mm is considering the sensitivity of melt pool depth (50–60 μm) and grain size as well as the stability of the cutting process. The cutting-edge radius and cutting tool width are 0.02 mm and 4 mm respectively. To observe the grain responses before and after machining, the experimental process is shown in Fig. 3c–h. Firstly, each test piece was polished and then marked at the centreline of the workpiece by scriber of height gauge. This is finished by fixing the sample on a flat stage and then moving the height gauge to scratch. And then the sample is rotated 90° for another perpendicular scratch. The distance of the marked line from the top free surface (Fig. 3e) is set as 2.5 mm for two reasons: (1) both the mark and free surface could be directly captured in a single SEM image under low magnification, reducing the error caused by specimen stage motion; (2) the marked line of such distance would not deform and not affect EBSD signal after cutting. It is helpful to ensure that the EBSD scanning is in the same area before and after cutting. The centreline mark on the polished sample was used as the reference to locate the EBSD mapping area before and after cutting. Secondly, a 1 mm × 1.2 mm EBSD mapping window was chosen to obtain the crystallographic microstructure of the material before cutting, as highlighted by the blue rectangle and evidenced in Fig. 3f. After obtaining the EBSD data of the “non-cut sample”, the observed piece was machined with 400 μm cutting depth (pre-cutting) to remove the surface layer. This is to form a slight curve that matches the pendulum motion path. This curve can ensure the stability of real cutting process. Then 200 μm cutting depth (real-cutting) is conducted for experimental investigation, as depicted in Fig. 3g. Finally, without second polishing, the machined workpiece was directly subjected to the EBSD characterisation at the exactly the same zone as shown in Fig. 3h. In order to guarantee the success rate of this test, no repeated cutting test was implemented for the polished sample and the cutting force was only measured at once. The cutting force analysis was not included in this work.

2.4. Microstructure characterisation

To examine the microstructure and crystallographic textures on different surfaces (top surface and adjacent side surfaces) of 0°, 67°, and 90° rotations, samples were cut parallel and perpendicular to (BD) by wire EDM. The samples were successively ground and polished to 1 μm surface finish. Etchant-Acetic Glyceregia (15 ml HCl, 5 ml HNO_3, 10 ml acetic acid and 2 drops glycerol)-was prepared to etch every sample for about 15s. The microscopic characteristics such as melt pool size and morphology were studied by optical microscopy whilst the microstructure characteristics such as phase distribution, grain morphology and orientation were investigated by SEM and EBSD. The samples for the EBSD characterisation also underwent a careful mechanical/chemical polishing stage to achieve 0.03 μm surface finish with minimum surface deformation through Vibratory Polisher (PRESI VIBROTECH 300) using Suspension SPM (colloidal silica) for 8 h. A ZEISS Gemini SEM 300 equipped with a Bruker EBSD detector was used to characterise the microstructure of Alloy 718 after etching at an accelerating voltage of 15.0 kV by secondary electron imaging. The EBSD mappings for the as-built Alloy 718 samples before and after cutting were performed at a step size of 0.5 μm and 1.0 μm for high and low magnification respectively. And the EBSD data was post-processed by MTEX [31].

2.5. The Taylor-based plastic deformation model

To investigate the crystallographic texture-based deformation, a Taylor-based plastic model was used to evaluate the relationship between the shearing of Alloy 718 workpieces and crystal orientation [32]. According to the minimum energy theory proposed by Taylor, accomplishing a general deformation needs five independent slip systems and the one with a minimum sum of internal work in a crystal will be active. In an FCC metal, there are four slip planes, and each plane has three slip directions as shown in Table 2.

The schematic of orthogonal cutting is shown in Fig. 4, in which the cutting tool is perpendicular to the cutting direction (CD), and the chip is removed under the shear stress in the shear plane (SP) conditions [33]; this is influenced, among other parameters, by the cutting tool geometry and cutting direction. The shear plane (SP) is parallel to the shear direction and recognised as a 2D plane (the normal of shear plane is perpendicular to the shear direction). Since the ratio of cutting depth to cutting-edge radius (h/r) is approximately 10, it can be inferred that the cutting process is relatively insensitive to the cutting-edge radius [34]. In this study, the cutting tool is considered to be perfectly sharp and the effect of cutting-edge radius on the deformation is disregarded. Moreover, in accordance with the assumption of plane strain during orthogonal cutting, the cutting tool width (4 mm) is chosen to be four times wider than the workpiece [33].

The Taylor-based model can calculate the shear deformation gradient ($\in_{shear}$) in the SP with the plane-strain condition [32]:

$$\in_{shear} = \frac{d\varepsilon}{2}\begin{pmatrix} 0 & 1 & 0 \\ 1 & 0 & 0 \\ 0 & 0 & 0 \end{pmatrix} \tag{1}$$

The deformation gradient and frame transformation are in Appendix A.

To calculate the most active slip trace for each grain in the FCC structure and the grain boundary effect is not considered in this model, the deformation gradient $\in^{crystal}$ is based on five independent slip systems and can be written as:

$$\in^{crystal} = \sum_{\alpha=1}^{5} m^{\alpha}\delta\gamma^{\alpha} \tag{2}$$

where $m^{\alpha} = b^{\alpha} \otimes n^{\alpha}$, b^{α} is slip direction for slip system α, n^{α} is the slip plane normal for slip system α, $\delta\gamma^{\alpha}$ denotes shear increment at slip system. It should be noted that the five independent slip systems here are employed to calculate the minimum work in slip system. This does not means that five slip system will be observed in real plastic deformation. The deformation occurs with minimum energy and the work increment, δw can be written as:

$$\delta w = \tau_c \sum_{i=1}^{5} \delta\gamma \tag{3}$$

Table 2
Slip planes and corresponding slip directions for FCC metals.

Slip plane, n	(111)			($\bar{1}\bar{1}1$)			($\bar{1}11$)			($1\bar{1}1$)	
Slip direction, b	$[01\bar{1}]$	$[\bar{1}01]$	$[1\bar{1}0]$	$[0\bar{1}\bar{1}]$	[101]	$[\bar{1}10]$	$[01\bar{1}]$	[101]	$[\bar{1}\bar{1}0]$	$[0\bar{1}\bar{1}]$	$[\bar{1}01]$	[110]

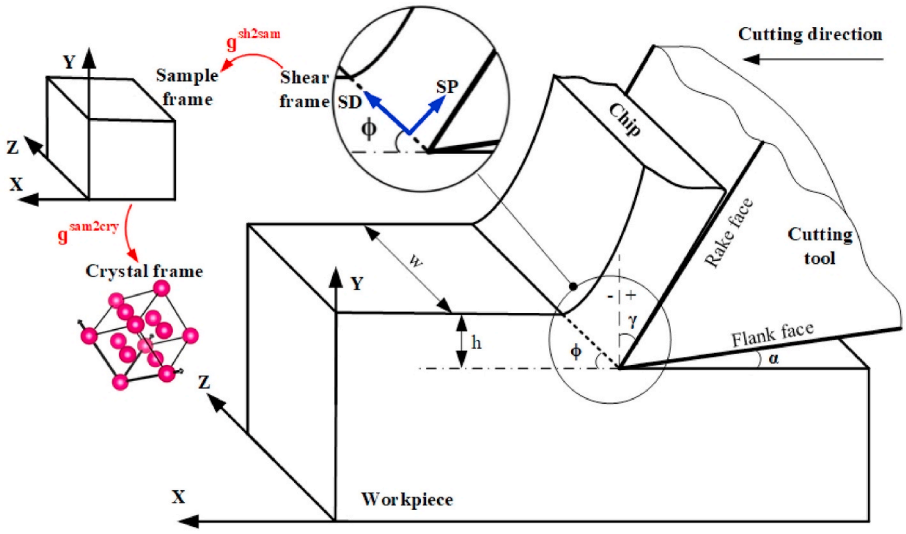

Fig. 4. Orthogonal cutting model and the frame relationship among shear plane, sample and crystal. Shear direction (SD) and shear plane (SP) are shown as blue arrows.

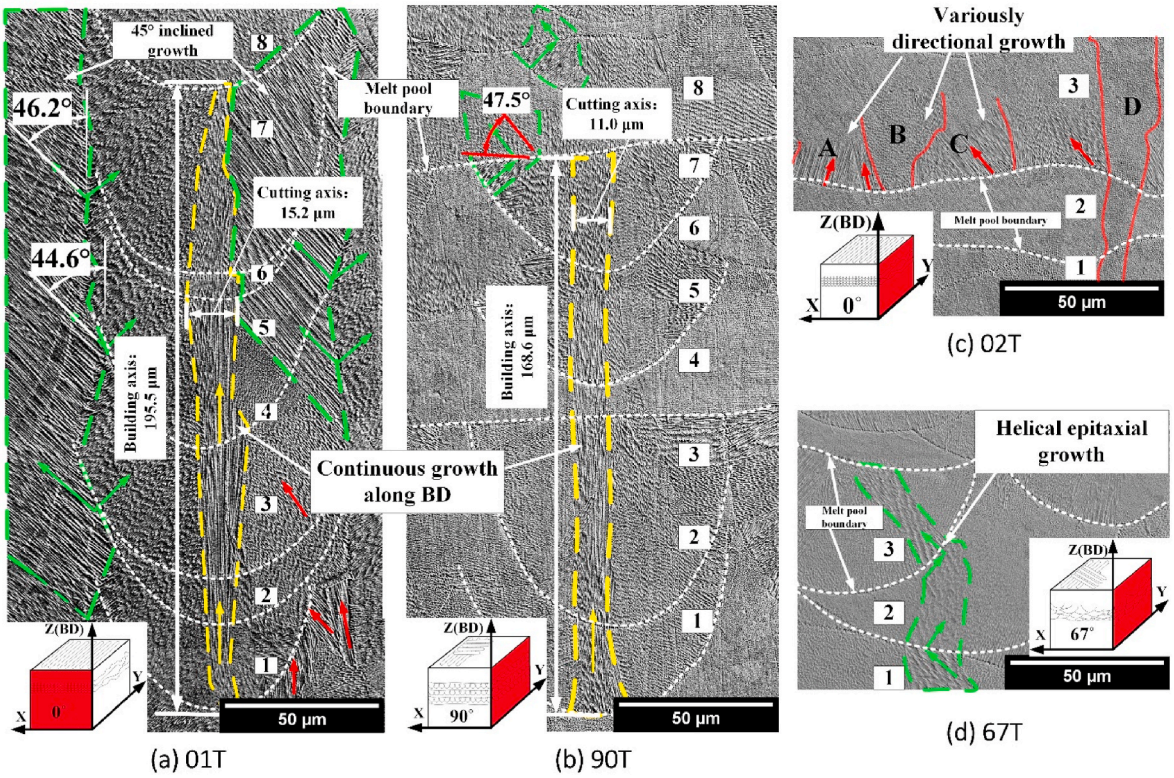

Fig. 5. Representative microstructures for three scanning strategies (0°, 90° and 67°). (a) The build direction (BD) is along the z-axis (see inset); the continuous growth of cells across several layers along the centre line of melt pools (highlighted by yellow dashed line) and the side-branching epitaxial growth with about 45° to BD according to the measured values (highlighted by green dashed line) in 01T; (b) Continuous growth along BD (see inset) in 90T and side-branching at the side of melt pools; (c) Various cell growth directions within a melt pool; (d) Side-branching growth at the side of the melt pool. The coordinate system and scanning strategies are in the inset, and observing surfaces are marked in red. Cell growth directions are marked with arrows.

The detailed slip trace calculation is detailed in Appendix A and B.

Therefore, how the initial crystallographic textures of the as-built structures will respond to cutting and how the deformation will be altered after cutting can be investigated.

To identify the slip trace in the SEM image, slip traces corresponding to all four slip planes is calculated based on original Euler angles before cutting. It can be conducted by cross product of slip plane normal with the sample frame (i.e., Y direction in sample frame). All slip traces in four samples are computed as shown in Fig. S3. The detailed computing is in Appendix B.

2.6. Full-field crystal plasticity simulation model

The simulation of the crystal response to the orthogonal cutting process is carried out using a well-established framework based on resolved shear stress, which was originally proposed by Hill, Rice, and many others [35]. The deformation gradient, $\boldsymbol{F}$, can be written as:

$$\boldsymbol{F} = \boldsymbol{F}^{*} \bullet \boldsymbol{F}^{p} \tag{4}$$

where $\boldsymbol{F}^{*}$ is caused by stretching and rotation of crystal lattice with reference to the intermediate configuration and $\boldsymbol{F}^{p}$ is the deformation due to plastic shearing on crystallographic slip systems. The crystallographic calculation model for FCC is detailed in Appendix C, including material parameters, boundary condition and post-processing dealing with visualization of stress status. The geometry model for meshing and simulation is obtained from EBSD data before cutting, which ensures the loading is applied to original grains. The validation of simulation results is accomplished by comparing them with the plastic deformation captured by SEM.

3. Results

3.1. Representative microstructure of the as-fabricated alloy 718

The epitaxial growth microstructure of the Alloy 718 built by parameters in Table 1 is presented in Fig. 5, whereby the coordinate system for the as-built sample is given in the inset and observing surfaces are marked in red. The scanning strategy changes laser path directions to provide a unique thermal pattern for grain growth. The thermal pattern finally generates identifiable grain characteristics as shown in Fig. 5. In the micrographs, plenty of cells (smallest unit in the melt pool with size of 0.5–3 μm) are formed due to quick solidification. They are marked with dashed lines and arrows to indicate the growth direction, and the printed layers are numbered (layers 1–8) in Fig. 5a. The continuous growth of cells across several layers (Layers 1–8 in Fig. 5a) along BD is only found in 01T and 90T. Their grain lengths (building axes) along the building direction reach 195.5 μm and 168.6 μm as shown in Fig. 5a and b respectively. Both continuous epitaxial growths occur at the centre of melt pools and their growth directions are along BD, exhibiting a slender and elongated morphology. However, the grain widths (cutting axes) along the cutting direction in 01T and 90T are less than 20 μm, leading to a high aspect ratio (building axis to cutting axis). Side-branching frequently occurs at the side of a melt pool in 01T with an inclined angle of about 45° to BD, crossing four layers (layers 4–8), as shown by the green dash lines in Fig. 5a. The cell growth direction is nearly perpendicular to cells in neighbouring melt pools following green arrows in Fig. 5a. However, the complex molten flow in the melt pool can also disturb the 45°-inclined growth pattern (measured in Fig. 5a) at the side of melt pools, resulting in various cell growth directions as shown in layers 1–4 (red arrows). In addition, the 45° inclined side-branching is likely to grow towards the centre of the melt pools, restricting the growth of the build-directional continuous cells. This is indeed seen in Fig. 5a that the growth of continuous cells is limited in layers 5–8.

In Fig. 5b, laser scanning directions are perpendicular in adjacent layers, leading to 90°-rotational melt pools in neighbouring layers. For example, layer 3 is along the Y-axis and layer 4 is along the X-axis, according to the coordinate system in each inset. In the 90°-rotation strategy, the cells that grow at the side of a melt pool are disrupted by the subsequent layers as measured between layers 7 and 8, inhibiting the 45° inclined side-branching growth. Various cell growth directions can be found in a single melt pool of 02T (layer 3 in Fig. 5c). Cell growth directions in 02T are nearly normal to the melt pool boundary (white dashed lines), but localised growth directions are different as shown in zone A, B and C (red arrows) in Fig. 5c. The growth direction of cells across different layers (layer 1–3) in zone D is in the same direction (out of the plane). It should be noticed that the side-branching growth (green arrows) was not found in 02T from Fig. 5c. This is because the out-of-plane directional growth is hard to track in a 2D figure. In the 67° (67T) built direction, as shown in Fig. 5d, the laser scanning direction rotated 67° in every subsequent layer, breaking the continuous growth of cells at the centre of the melt pool. The growth direction of the cell highlighted by a green dashed line is interrupted by the melt pool boundary (MPB) in layer 1, but the growth direction changed about 90° in layer 2 and another 90° in layer 3, resulting in the helical epitaxial growth pattern.

3.2. Crystallographic textures and slip systems exposed to machining tests

Fig. 6a–c presents the inverse pole figure (IPF) cubes of Alloy 718 printed by three scanning strategies. EBSD data was obtained from three orthogonal planes (XY, XZ, and YZ) and then merged to create 3D cubes for each of the three cases. However, it should be noted that the resulting cube represents a combination of three IPF maps rather than a true 3D grain structure. Due to the unchanged scanning direction in the 0° rotation strategy, microstructure in the XZ and YZ planes are different Fig. 6a. In contrast, since the scanning direction rotated 90° and 67° in each layer, the microstructures in XZ and YZ planes (Fig. 6b and c) are equivalent in these two cases. The build direction is shown in the coordinate system and grain boundaries with a misorientation angle larger than 15° are identified as large-angle grain boundaries. The workpieces used in this work are taken from side surfaces as marked with black rectangles. It should be noted that grains in the selected regions have typical size, shape and orientation in each sample.

The grain morphologies are highlighted in Fig. 6a1-c1. In Fig. 6a1, the slender elongated grains (zone 1) correspond to the previous build-directional continuous cells in Fig. 5a. Since the Alloy 718 exhibits an FCC structure, the grain orientation is not changed although the cell's growth direction changes to 90°. Therefore, the mentioned vertical growth cells in neighbouring melt pools in Fig. 5a (green arrows) at the side of melt pools are from the same grain, forming the <011>-columnar grains (Zone 2) in Fig. 6a1. Various cell growth directions induced by perturbation in the melt pool result in the fine-grain zone as shown in Zone 3 from Fig. 6a1. Grains in 02T (Fig. 6a2) are nearly along BD, which matches well with cells in Fig. 5c that grow roughly normal to the melt pool boundary. The orientation varies in the highlighted area in Fig. 6a2 due to the inclined cell growth within a melt pool, while large grains are found because of the same growth direction in several layers. The slender elongated grain formed by build-directional continuous cells is also observed as highlighted by the black rectangle in Fig. 6b1, which corresponds well to build-directional continuous cells in Fig. 5b. In Fig. 6c1 of 67T, the helical epitaxial growth cells result in zigzag-shaped grains in the 2D plane and the grain growth direction inclined angles against the BD. The non-repeatedly rotational scanning strategies randomise cell growth direction, resulting in various orientations and smaller grain sizes than the other three samples in Fig. 6c1.

Fig. 7 shows the corresponding crystallographic texture of the samples mentioned in Fig. 6a1-d1 and the lattice orientation as well as the possible slip systems. It should be noted that the intensities and orientations in these four selected regions (0.4 mm × 0.4 mm) are similar to those in the 1.2 mm × 1.2 mm regions, as shown in Supplementary Fig. S1. This indicates that these four selected regions can represent the

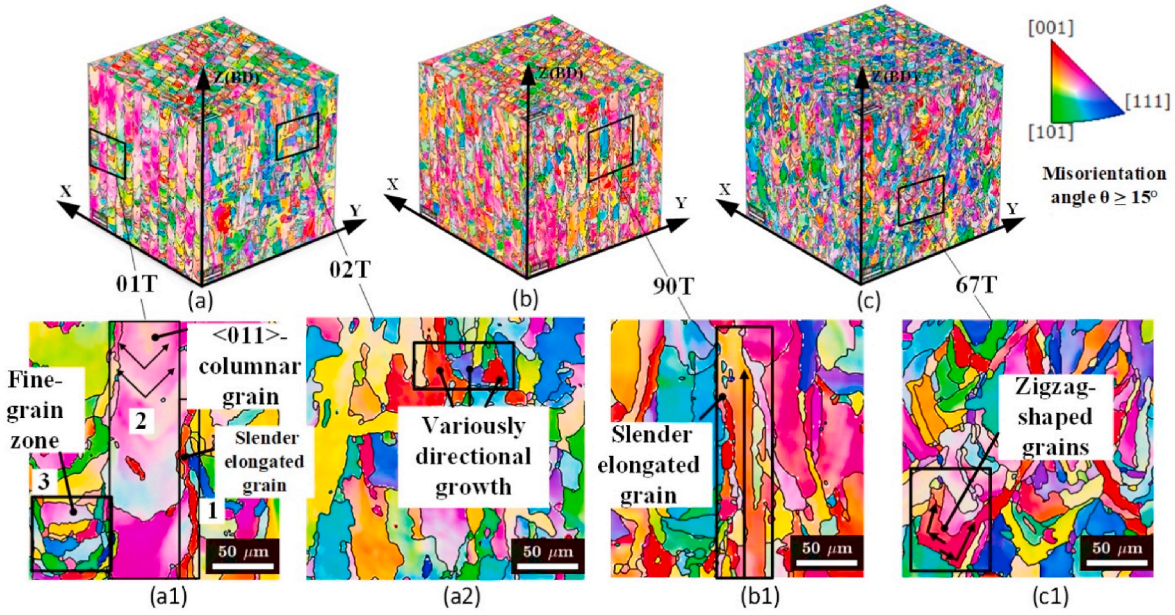

Fig. 6. IPF maps acquired from XY, XZ and YZ planes for three scanning strategies. (a) 0° rotation; (b) 90° rotation; (c) 67° rotation. IPF of machining areas were selected by black rectangles for (a1) 01T, (a2) 02T, (b1) 90T and (c1) 67T (grain growth patterns are marked with arrows).

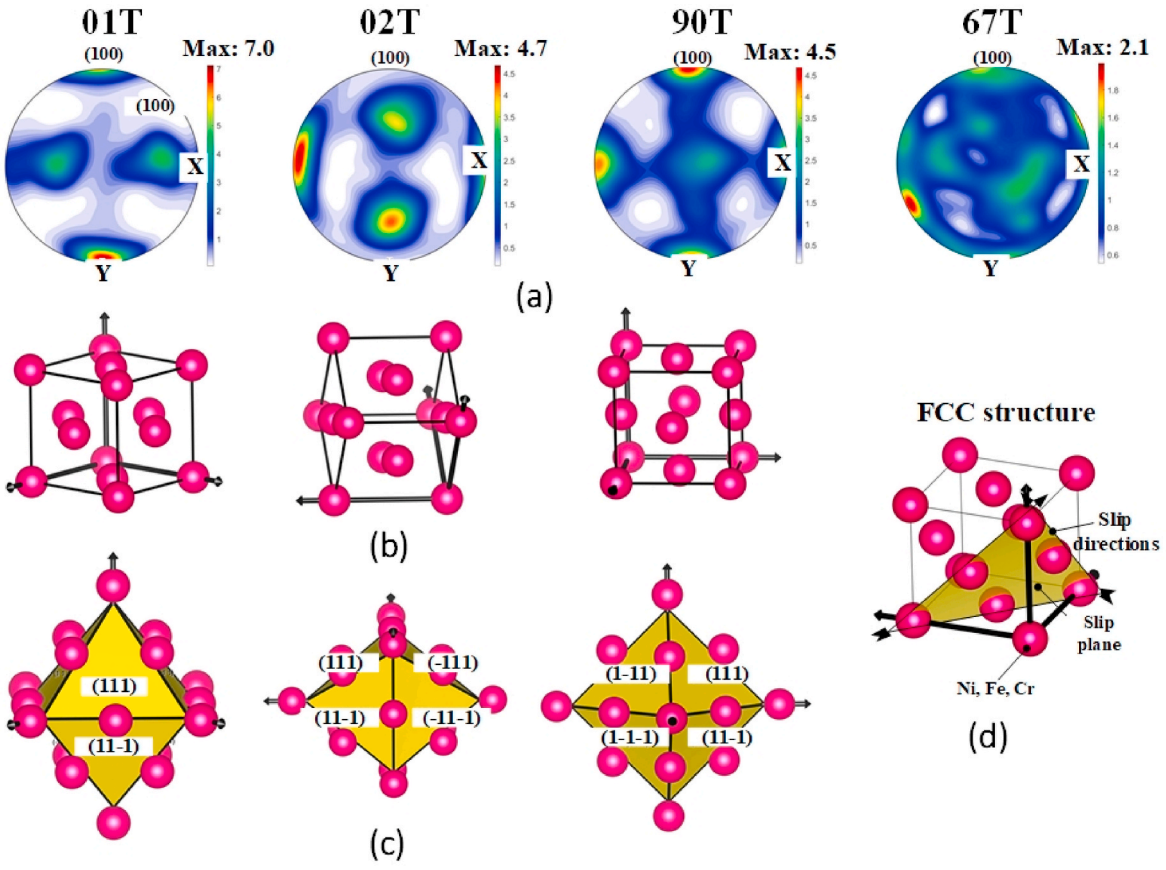

Fig. 7. Pole figures (PF), corresponding lattice structures and slip systems for four samples. (a) Corresponding crystallographic textures in the XZ planes (YZ plane for 02T) (the {011} and {111} pole figures can refer to Supplementary Fig. S1.); (b) Different FCC lattice orientations for textured specimens; (c) Corresponding textured close-packed slip system in FCC (the texture of 67T was too weak to show distinctively textured lattice structure and slip system); (d) illustration of slip plane and slip directions in an FCC structure.

four textured Alloy 718 samples.

According to {100} pole figure in Fig. 7a, only 01T, 02T and 90T presented significant textures, but the texture of 67T was too weak to be identified due to the 67°-rotation scanning strategy. In 01T, <011>//BD and <001>//BD textures are observed, in which the <011> texture is caused by 45° inclined cells (as seen in Fig. 5a (green arrows)) and the <001> texture is attributed to those continuous growth cells with <001> growth direction at the centre of a melt pool. This texture is consistent with previously reported studies [36,37]. A <011> texture along to Y-axis was obtained in 02T, of which the maximum intensity was 4.5, lower than 7 in 01T. A strong cube texture of three <001> aligned to X, Y and Z (BD) was obtained in 90T, which is in good agreement with previous studies for FCC metals with the same scanning strategies [38]. The maximum texture intensity of 67T was only 1.9 and no preferred grain orientations were found due to the non-repeated laser scanning rotation in every layer. The large area corresponding {001} {011} and {111} pole figures can refer to Supplementary Fig. S1.

Considering the symmetry of FCC alloy, the lattice orientations of representative grains in the textured Alloy 718 are shown in Fig. 7b by oriented cubes to reflect the texture in Fig. 7a. And the illustration of the FCC lattice structure and slip system is shown in Fig. 7d. The red balls represent the metal atoms (Ni, Fe or Cr in this case) that form the FCC structure, and the yellow plane is the slip plane. Every slip plane has 6 slip directions marked with black arrows. Based on this illustration, Fig. 7c presents corresponding slip planes and slip directions for 01T, 02T and 90T based on the crystallographic texture in Fig. 7a. It should be noted that the preferred lattice structure and slip system are not depicted in 67T due to its weak texture.

3.3. *Quasi-in-situ observation of machining induced plastic deformation of the crystallographic textured workpiece built by three scanning strategies (0°, 90° and 67°)*

The grain deformation after orthogonal cutting was investigated via EBSD and SEM. Since the plastic deformation leads to poor Kikuchi pattern quality in chips, the chip deformation before and after cutting is not included in this work. It is noted that the EBSD data is fitted to reduce the noise of scratches. Since the de-noise step is small, the orientation and grain structure near the machined surface are not changed. The inversed pole figures (IPFs) of 01T before and after machining are presented in Fig. 8a and b. Several build-directional blocks are observed as shown by the dashed lines and slender elongated grains are between the build-directional blocks. To trace the evolution of individual grains before and after cutting, deformed grain A′ and Grain B′ are compared with original Grain A and Grain B. It can be seen from Fig. 8d that Grain A and Grain B were slightly curved along the cutting direction. It should be noticed that the edge in Fig. 8b is not the machined surface but the EBSD detectable area beneath the machined surface as the Kikuchi pattern in the machined surface is difficult to index due to significant deformation. However, there is much less deformation in the other three samples and the Kikuchi patterns are detectable near the machined surface. The deformation of Grains A′ and B′ still follows shear condition but the strain is not as large as the region near the machined surface [39]. The effect of temperature is disregarded in this study due to the relatively short total cutting time of approximately 220 μs. Additionally, the heat accumulation is expected to be minimal due to the small dimensions of the workpiece (cutting length: 6 mm, sample thickness: 1 mm) and the presence of adiabatic shear bands in the primary shear zone would not significantly impact the deformation of machined surface.

According to the characteristic bugling retained on the observation surface (Fig. 8d), the deformed grains in the SEM image are linked with corresponding grains in the IPF as shown in Fig. 8b, d. In this way, the machining-induced deformation can be analysed based on grain morphologies and orientations. A similar deformation structure is observed (Fig. 8c, dashed lines) based on these typically repeated bulges, which matches well with the build-directional blocks in Fig. 8a (black dashed lines). Due to the retained bulges on the surface, this is the first time that the similar deformed structure is reported in as-built LPBF structures (i.e. Alloy 718) during the shear-based deformation. The spacing of the similar structures (71.1 μm and 77.9 μm in Fig. 8d) is close to the spacing of the melt pools (72.3 μm and 71.6 μm) in Fig. 8e, suggesting the similar

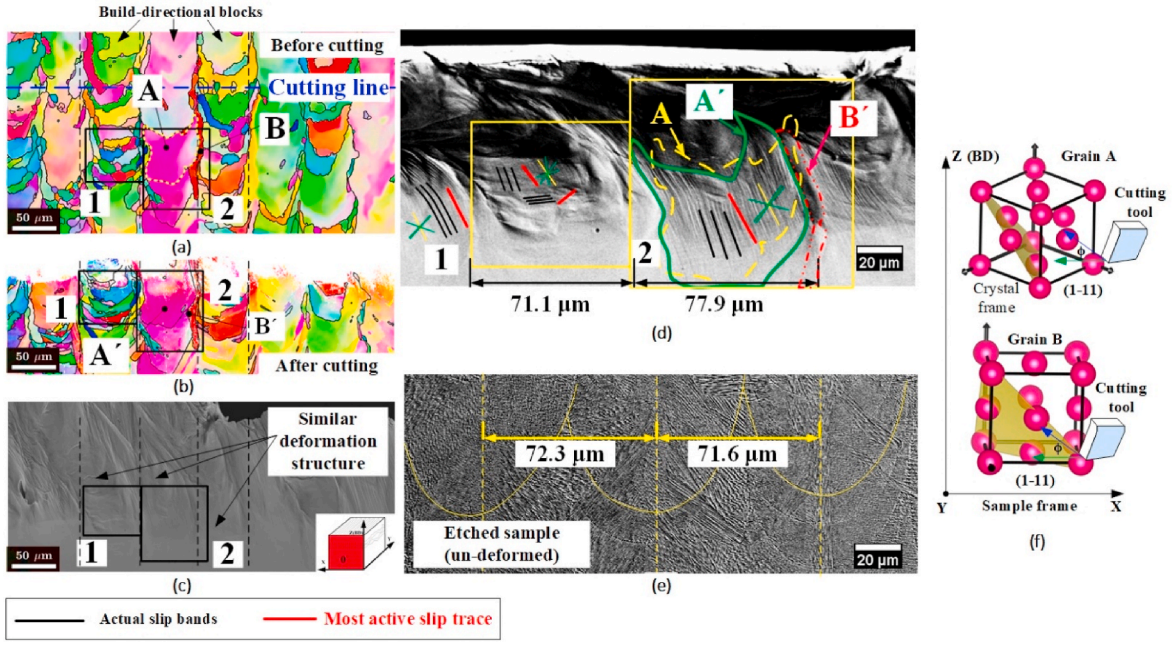

Fig. 8. Quasi-in-situ observation of 01T. (a) Before orthogonal cutting; (b) after orthogonal cutting; build-directional blocks was divided by dashed lines; (c) SEM image on the EBSD stage (70° inclined) and similar deformation structure was marked with arrows; (d) SEM image of selected Zone 1 and Zone 2; outlines of original Grain A and deformed Grain A′ were highlighted by yellow lines and green lines (the most active slip trace and actual slip bands were marked by red line and black line respectively; the plane traces are highlighted by dark green lines and the activated slip trace is marked by yellow line); (e) The centre line spacing in an etched sample; (f) The slip plane and cutting direction is shown in the sample frame.

structure is caused by slender <001>-elongated grains at the centre of melt pools and <011> columnar grains between the centre of each melt pool. The grain widths of columnar grains are approximately 50 μm, significantly wider than the slender elongated grains (about 10 μm). Since the cutting direction is parallel to the grain width direction, the deformation may be affected by such width difference. However, this similar deformation structure is not found in the other three samples due to the lack of a similar repeated grain along the cutting direction (e.g., build-directional blocks in 01T).

Euler angles (detailed in Supplementary Table S1) obtained from Fig. 8a (before cutting) was used to compute the slip trace, this can decrease the error caused by distorted grain and lattice rotation near the machined surface as shown in Fig. 8b. It can only be implemented due to the carefully collected grain information before cutting.

Grains in zone 1 and 2 from Fig. 8b are tracked in an un-etched SEM image (Fig. 8d) after cutting. The most active slip trace and actual slip bands were marked with red and black lines respectively. The relationship between representative FCC structures and machining direction is shown in the sample frame in Fig. 8f. The cutting direction is along the green arrow and the shear direction is along the blue arrow. The angle between the cutting and shear direction is the shear angle (φ). According to the diagram of the cutting tool and FCC structure of Grains A and B (Fig. 8f), the most active slip trace in Grain A is nearly parallel to the shear direction whilst there is a spatial angle between the slip plane in Grain B and shear direction. The detailed Euler angles and slip planes are listed in Supplementary Table S1.

The traces of different slip planes are distinguished for the FCC structure with four slip planes. This can be done by comparing the visible slip bands in the SEM images with the four traces extracted from EBSD data (Fig. S3 in supplementary). Four {111} plane traces are highlighted by green lines and the activated slip trace is marked by yellow lines (Fig. 8d). The same mark is also used in following three cases for slip trace analysis. Typical intensive slip bands are dominated in Grain A′, which is nearly parallel to the shear direction. A significant squeezing-out effect is likely found in Zone 1 (fine grain zone) and build-directional block boundary (e.g., Grain B), indicating that narrow grain width (cutting axis) along the cutting direction may lead to significant inhomogeneous deformation.

Fig. 9a and b shows the IPFs before and after deformation for 02T. The relationship between representative FCC structures of grains and machining direction is shown in the sample frame. The dominated slip bands are marked with black lines. By comparing Grain A and A′, the lattice rotation is observed in Grain A′ (Fig. 9b). It can be seen from Fig. 9e that grain bulging occurs near the machining surface due to the

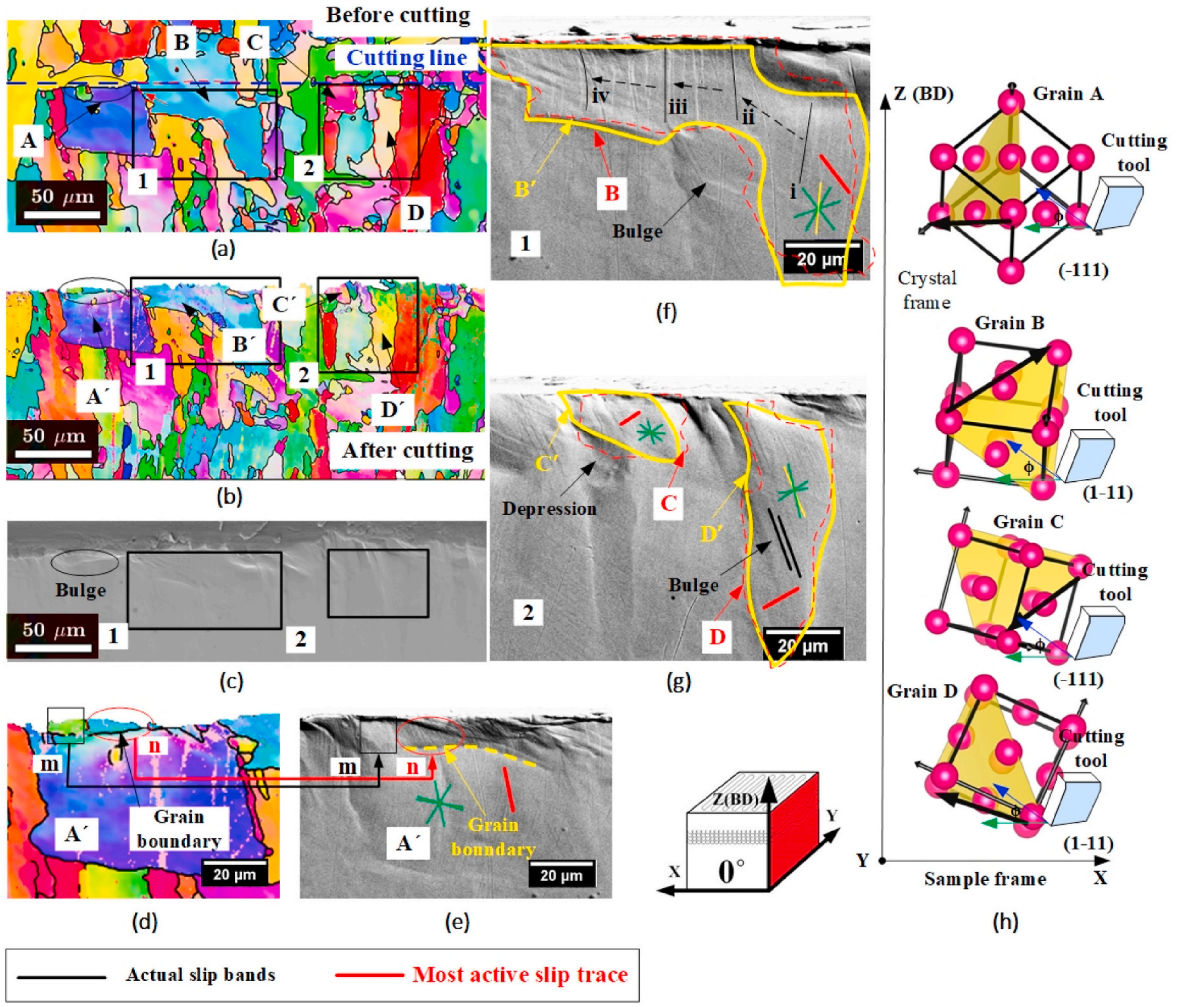

Fig. 9. Quasi-in-situ observation of 02T. (a) Before orthogonal cutting; (b) After orthogonal cutting (c) SEM image on the EBSD stage (70° inclined) and a bulge causing orientation change was marked with circle; (d) The orientation change in Grain A′; (e) the corresponding Grain A′ in observed by SEM; (f) SEM image of selected zone 1; the outlines of the original Grain B and the deformed Grain B′ were highlighted by red dashed line and yellow line; and slip bands evolution were marked with i to iv; (g) SEM image of selected zone 2, grain deformation was highlighted by red and yellow line and a bulge and a depression were marked with arrows; (h) Corresponding slip system and shear direction are presented in the sample frame (the most active slip trace and actual slip bands were marked with red line and black line respectively and the plane traces are highlighted by dark green lines and the activated slip trace is marked by yellow line).

low constraint in the free surface (YZ plane), causing the grain orientation change as highlighted by the red circle in Fig. 9d. The pink line across the grain is the scratch caused by sample fixation rather than twin or sub-grain boundary because the disorientation near this region is only about 1.4°. The grain boundary matches well with the corresponding counterpart retained in Fig. 9e. The lattice rotation is not limited in the observation (YZ) plane and the new grain boundary may be attributed to material pile-up. The high angle grain boundary may change the local stress status and impede slip transfer to the bulk. This is verified by different slip intensive in Grains n and A′. The local strain incompatibility near the grain boundary [40] causes slight lattice rotation in Grain A′, as shown in Fig. 9d. To the authors' best knowledge, there is no research that reported this phenomenon in the orthogonal cutting process and this has been observed based on our quasi-in-situ grain evolution analysis method.

A large grain and several fine grains were deformed as shown in Zone 1, 2. Grain B′ is slightly deformed compared with original Grain B. In Fig. 9f, Grain B′ is highlighted by the yellow dashed line, which matches well Grain B′ in Fig. 9b. The original Grain B is also marked in Fig. 9f according to Grain B in Fig. 9a. The roughly overlapped outlines of Grain B and B′ indicate that slight deformation occurred in Grain B. The slip bands are slightly inclined to the right (i), then gradually inclined to the left (ii and iii) and finally become curved (iv) in Fig. 9f. This slip bands evolution phenomenon indicates that the strain gradients near the grain boundaries is more significant than the centre of Grain B′. In Fig. 9g, there are no intensive slip bands in Grain C′ compared with original Grain C due to the small grain size. Comparing the outlines of Grain D and D′ in Fig. 9g, the grain causes a larger deformation depth than the small grain nearby. This indicates that the grain deformation is dependent on the grain morphologies (i.e., grain width) in the machining process.

In Fig. 10a–c of the 90T sample, Zone 1 is selected to analyse the deformation of elongated grains. The grain orientation of the upper region of Grain A and B is changed after deformation as compared to that of Grain A′ and B′ in Fig. 10b. In Fig. 10d, Grain A′ is inclined according to the outlines of Grains A and A′, and the wrinkling is found within the grain, corresponding to the orientation change in Fig. 10b. Similarly, the wrinkling also exists in Grain B′, leading to the local orientation change in Grain B′ (Fig. 10b). In Fig. 10e, slip bands transmit from Grain D′ to Grain C′ with high compatibility between two grains (i.e., slip band direction is not changed). And the grain boundary between the two grains is not inclined or curved, suggesting less plastic strain accumulation at the grain boundary. Multi slips are activated in Grains C′ and D′ and the slip bands are then hindered by the grain boundaries below. The multi slips in both Grains C′ and D′ may be attributed to the typical grain orientations (Grains C and D in Table S1). In such orientations, it may be easier for more than one slip system to exceed the resolved shear stress during cutting, resulting in the formation of multi-slip bands. Additionally, since Grains C and D have similar orientations, neighbouring grains with high compatibility (or lower misorientation) allow slips to cross the grain boundary with original slip directions [41]. It should be noted that Grains A′ and D′ have similar grain areas (about 2000 μm^2) and orientations (<001>//BD). But due to the different grain morphologies, intensive slip bands were only observed in Grain D′, whilst significant wrinkling occurred in Grain A′. This indicates that the cutting axis (grain width along the cutting direction, Fig. 10d) may be a better indicator for grain size estimation during the shear-based deformation, especially for the LPBF-fabricated grain with a high aspect ratio (building axis to cutting axis).

In Fig. 11a and b, the grain deformation of 67T is observed based on the typical shape of bulges, and grain features in Zone 1 and 2 matched well with Fig. 11c. The grain size of 67T is smaller than the previous three samples, resulting in more pronounced "wrinkling" near the machined surface as shown in Fig. 11c. In Fig. 11d, it is found that the boundary of Grain A′ is curved near the machined surface compared with its original outline, and slip bands only occur in Grain A′ as seen from Zone i and Zone ii in Fig. 11d but are not found in Grain B′. According to the most active slip traces marked with red lines and FCC structure of Grains A and B in Fig. 11f, the activated slip trace in Grain A′ is parallel to the shear direction while the trace of Grain B′ is

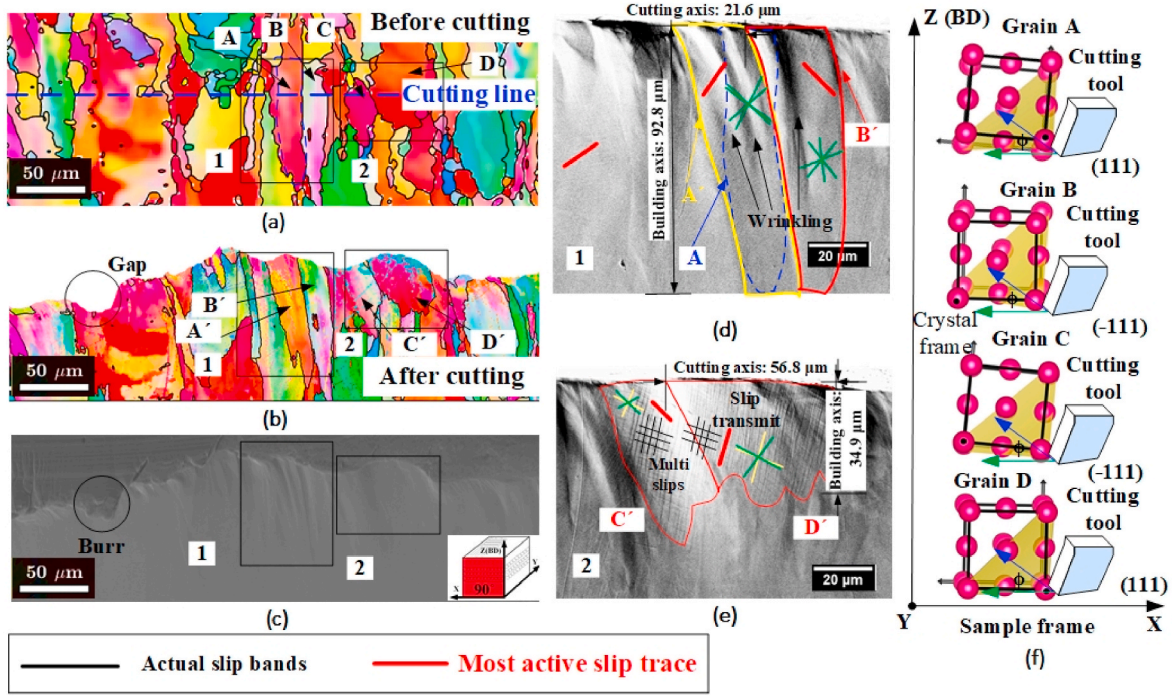

Fig. 10. Quasi-in-situ observation of 90T. (a) Before orthogonal cutting; (b) After orthogonal cutting; (c) SEM image on the EBSD stage (70° inclined); (d) Grain inclining and wrinkling within Grain A′ and B′; (e) Slip transmitted across the grain boundary between Grain C′ and D′ as well as multi slips in Grain C′ (long and short axes were marked); (f) Corresponding slip system and shear direction are presented in the sample frame (the most active slip trace and actual slip bands were marked with red and black lines respectively and the plane traces are highlighted by dark green lines and the activated slip trace is marked by yellow line).

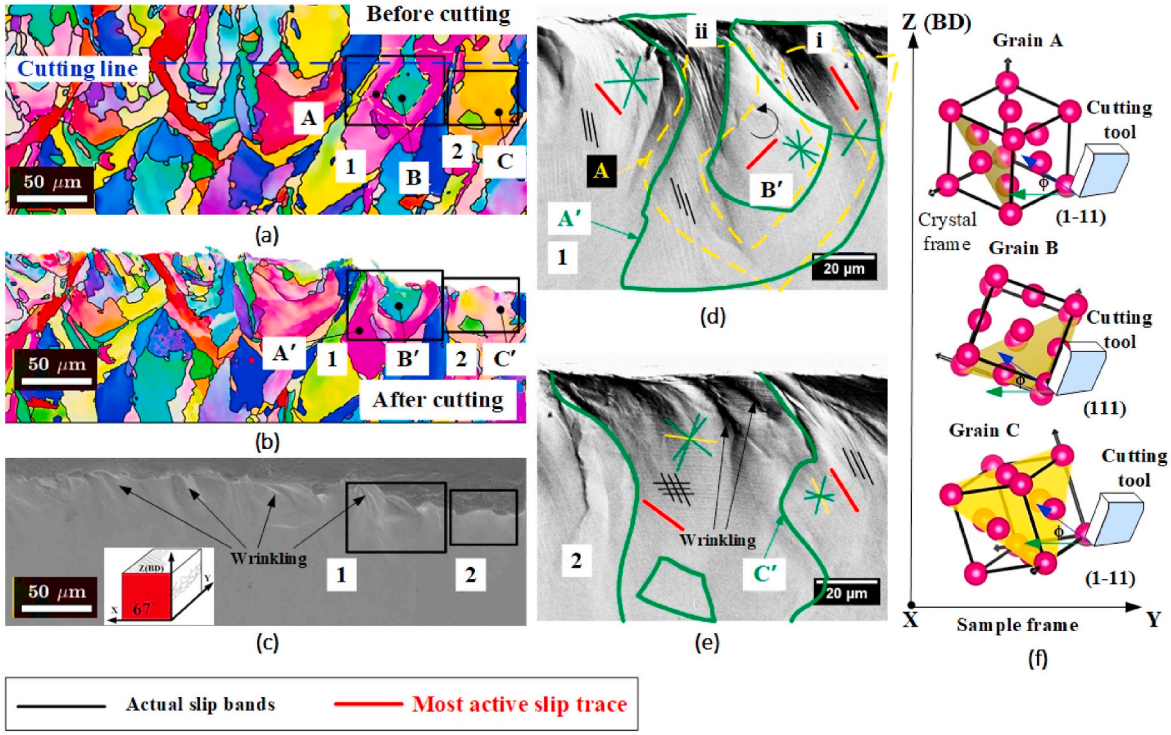

Fig. 11. Quasi-in-situ observation of 67T. (a) Before orthogonal cutting; (b) After orthogonal cutting; (c) SEM image on the EBSD stage (70° inclined) and the wrinkling was marked with arrows; (d) SEM image of selected zone 1 and a grain rotation was observed in Grain B′; (e) SEM image of zone 2, the wrinkling occurred within Grain C′; (f) Corresponding slip system and shear direction are presented in the sample frame (the most active slip trace and actual slip bands were marked with red and black lines respectively and the plane traces are highlighted by dark green lines and the activated slip trace is marked by yellow line).

perpendicular to the shear direction. Thus, intensive slip bands are found in Grain A′ but the Grain B′ restricts the slip transmission and no slip bands are visible in Grain B. Moreover, the grain width near the machine surface is different in Grains A and B. In Fig. 11a, cutting line is through a very narrow part of Grain B but a relatively wide region of Grain A. Grain B may exhibit high deformation resistance due to the narrow grain boundary distance. Because such deformation is not only dependent on orientation but also grain morphology, the generally used indicator, for example Taylor factor or Schmid factor, may not be suitable to eliminate the grain formed by LPBF. It also indicates that the grain size in the cutting process may dependent on the grain width along the cutting direction. In Fig. 11e, non-homogenous deformation occurs

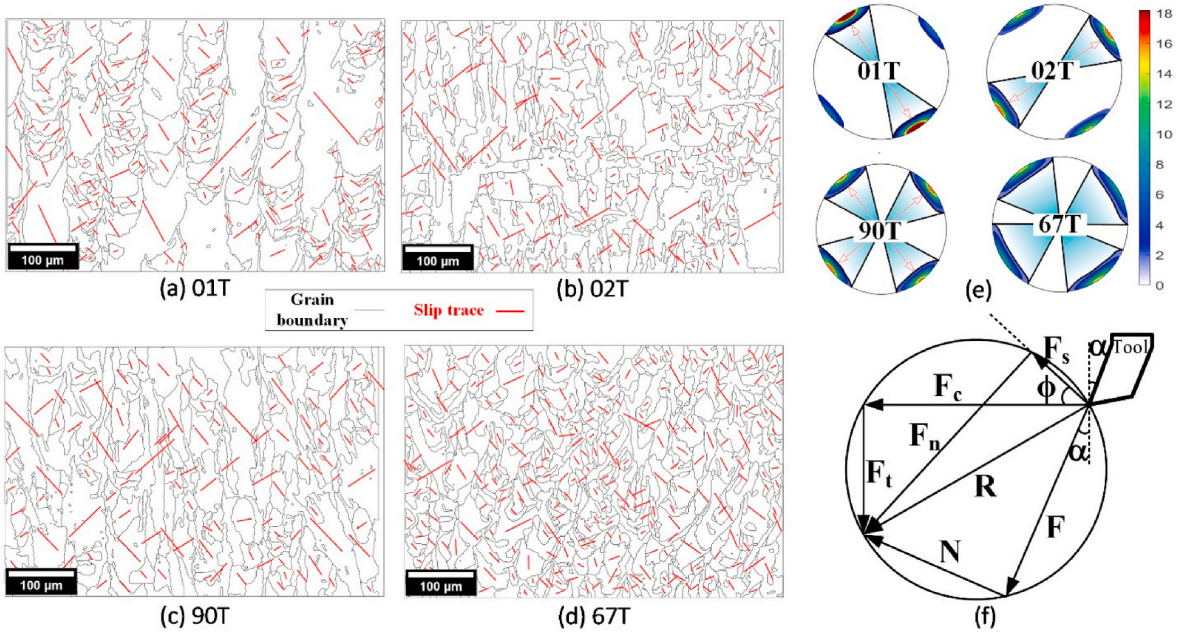

Fig. 12. Most active trace of slip plane based on Taylor-model. (a) 01T; (b) 02T; (c) 90T; (d) 67T; (e) The distribution of the most possible slip trace for each sample was calculated consider the grain size (the dominated slip trace was marked with red arrows); (f) The Merchant's Circle diagram (the detailed FCC slip traces for each grain can refer to Supplementary Fig. S3.)

within Grain C′, resulting in wrinkling and consequently orientation change near the machined surface.

3.4. The slip system in shear deformation based on the Taylor model

Since the textured deformation in Figs. 8–11 were dependent on typically oriented grains in four textured samples, the most active slip trace of each grain in a large-scale region for textured Alloy 718 was quantified as shown in Fig. 12a–d. According to the retained deformation history observed on the free surface, it is found that most individual grains are dominated by single directional slip bands whilst multi-slip bands only occurred in a few grains. This experimentally observational phenomenon contributes to building a new relationship between orientated grains and shear-based process via the most active slip plane. The slip trace is calculated in a 3D coordinate system to identify the activated slip plane. In order to visualise the slip trace in 2D grain maps, the intersecting line of the most active slip plane and grain map plane is presented in Fig. 12a–d, namely the most active slip trace (the detailed calculation is as shown in Section 2.5). According to the Taylor model, the most active slip trace can be calculated based on the shear strain imposed on each grain. It should be noted that the length of slip trace is normalised and multiplied by a grain size factor to match the actual grain size. The detailed FCC slip traces for each grain can refer to Supplementary Fig. S3. Since the large grain generally caused a larger area with similar slip trace directions than the small grain, the grain area was considered to calculate the slip trace intensity for each grain.

The intensity and direction of the most active slip trace for each textured sample are quantified in Fig. 12e, in which the activated slip trace for each grain was counted based on Fig. 12a–d. The slip traces are mainly distributed in blue shaded areas and the most possible slip traces are marked with red arrows. In this way, the orientation of each grain is transformed to the corresponding most active slip trace in the shear condition. The force in an orthogonal cutting system is depicted in Merchant's circle (Fig. 12f). The force R is the resultant of cutting force F_c and thrust force F_t. F_s is the shear force, α and φ are rake angle and shear angle, respectively.

Comparing the slip trace in Fig. 12e with the texture in Fig. 7a, the high texture intensity (01T in Fig. 7a) results in narrow distribution of slip traces. It is verified by the similar deformation structure as shown in 01T in Fig. 12a. And the weak texture intensity of 67T causes the wide distribution of slip traces as indeed seen in 67T of Fig. 12e. According to the slip trace distribution (shaded area and arrows) in Fig. 12e and the shear force (F_s) direction in Fig. 12f, it can be observed that the major activated slip traces in 01T are almost parallel to the shear direction due to <011>//BD texture. Interestingly, different from 01T direction the majority of slip traces in the 02T sample are perpendicular to the shear direction. This is because the <011> texture in 02T is nearly perpendicular to the BD, as shown in Fig. 7a, indicating more activated slip planes perpendicular to the shear force direction. Different angles between the shear force direction and the most active slip trace may lead to texture-based bulk deformation. From Fig. 12e, it is also observed that there are two representative traces of slip planes in the 90T sample, exhibiting a mixed manner of 01T and 02T. However, the slip traces in 67T are varied due to the weak texture and it is hard to find a representative slip system that is parallel or perpendicular to the shear direction. This can be attributed to the randomised grain orientation caused by the 67°-rotation strategy.

3.5. Full-field crystal plasticity simulations

In order to understand the complex deformation mechanism of the grains with different morphologies and orientations under machining conditions, full-field crystal plasticity simulation have been carried out with a well-established open source software [35].

The key aspect of this simulation is that it incorporates the grain orientation obtained from EBSD data prior to cutting and applies the corresponding loading resulting from the cutting operation; the detailed procedure is presented in Appendix C. In order to avoid the complexity associated with modelling the cutting process to extract the shear-based loading, we calculated the loading condition with an analytical model (Eq. (A1) in Appendix A) by considering cutting tool geometry and cutting depth and applied it to the region above the machined surface. Although the material removal process (e.g., chip formation) is not captured in this simulation, this limitation should not impact the analysis of machined surface deformation. Retaining the EBSD data before cutting allows for accurate loading application to the original grains and validation with SEM images.

Fig. 13 shows different intensities of stress and strain as well as corresponding deformation patterns in four cutting cases characterised by different grain morphologies and the two colour bars below represent Von Mises stress and equivalent strain values for four simulation cases. The stress values obtained in our study are in line with those reported works regarding the simulation of orthogonal cutting for Alloy 718 [42]. The simulated results are compared with the corresponding deformation pattern from SEM to investigate the mechanism of deformation based on stress and strain at the grain level. To optimise computation efficiency, the simulation region was a 400 × 90 μm area, as the deepest deformation zone in the experiment did not exceed 82 μm.

The simulation results indicate that local cutting-based plastic deformation depends on grain morphology and orientation as well as adjacent grains. In 01T samples (Fig. 13a), stress concentration is more likely to occur in <011>//BD columnar grains during cutting process, resulting in intensive slip bands observed at corresponding grains in Fig. 13c. However, the fine grain zone may interrupt such deformation pattern since grain boundary significantly hinders stress transfer from the machined surface to bulk and varies stress status to the next grain along the cutting direction. The stress concentration near the grain boundary leads to bulging instead of intensive slip bands crossing the grain boundary. The non-homogeneous deformation is found at each border of building directional blocks, causing similar deformation structure in Fig. 13c. Considering the predominant presence of columnar grains oriented along the <011>//BD direction in 01T, it is expected that these grains exhibit a notably similar slipping pattern as the calculated results in Fig. 12e (high intensity of slip trace direction distribution). These phenomena match well with the stress status in Fig. 13a. The highest equivalent strain is observed in 01T (Fig. 13e) compared with the other three cases, reaching about 0.8. The strain distribution is similar in each columnar grain but varies within the neighbouring narrow elongated grains. Such strain incompatibility caused by these two typical grains (i.e., columnar grain and narrow elongated grain) leads to localised inhomogeneous deformation as seen in Fig. 13c.

In 02T, the stress concentration is not significant as in 01T during the same cutting process. This is because grains in this case are dominated by < 011>⊥BD orientations and the most active slip trace is nearly perpendicular to the shear direction (Fig. 12e and f), leading to discrete slip bands and slight deformation as shown in Fig. 13d. It is also proved by the strain distribution shown in Fig. 13f, in which the strain value is lowest among these four cases.

Fig. 13g shows that the stress concentration is in elongated grains with <001>//BD orientation and the stress transfers to the bulk below. This leads to deeper deformation zones (red arrow in Fig. 13g) when compared with the neighbouring grains. The strain distribution of this grain (Fig. 13k) generally reduces from machined surface towards the bulk. Moreover, the strain transfer distance within this grain is deeper than in neighbouring grains, aligning with the deformation pattern in Fig. 13i. In Fig. 13g, stress concentration is not significant in the region where slip crosses the grain boundary. This implies that slip transfer across the boundary may occur in grains with similar orientation (as indicated in Table S1 for Grains C and D) during orthogonal cutting, thereby reducing the stress concentration near the boundary. Therefore, a slight deformation is observed in the corresponding region in Fig. 13g,

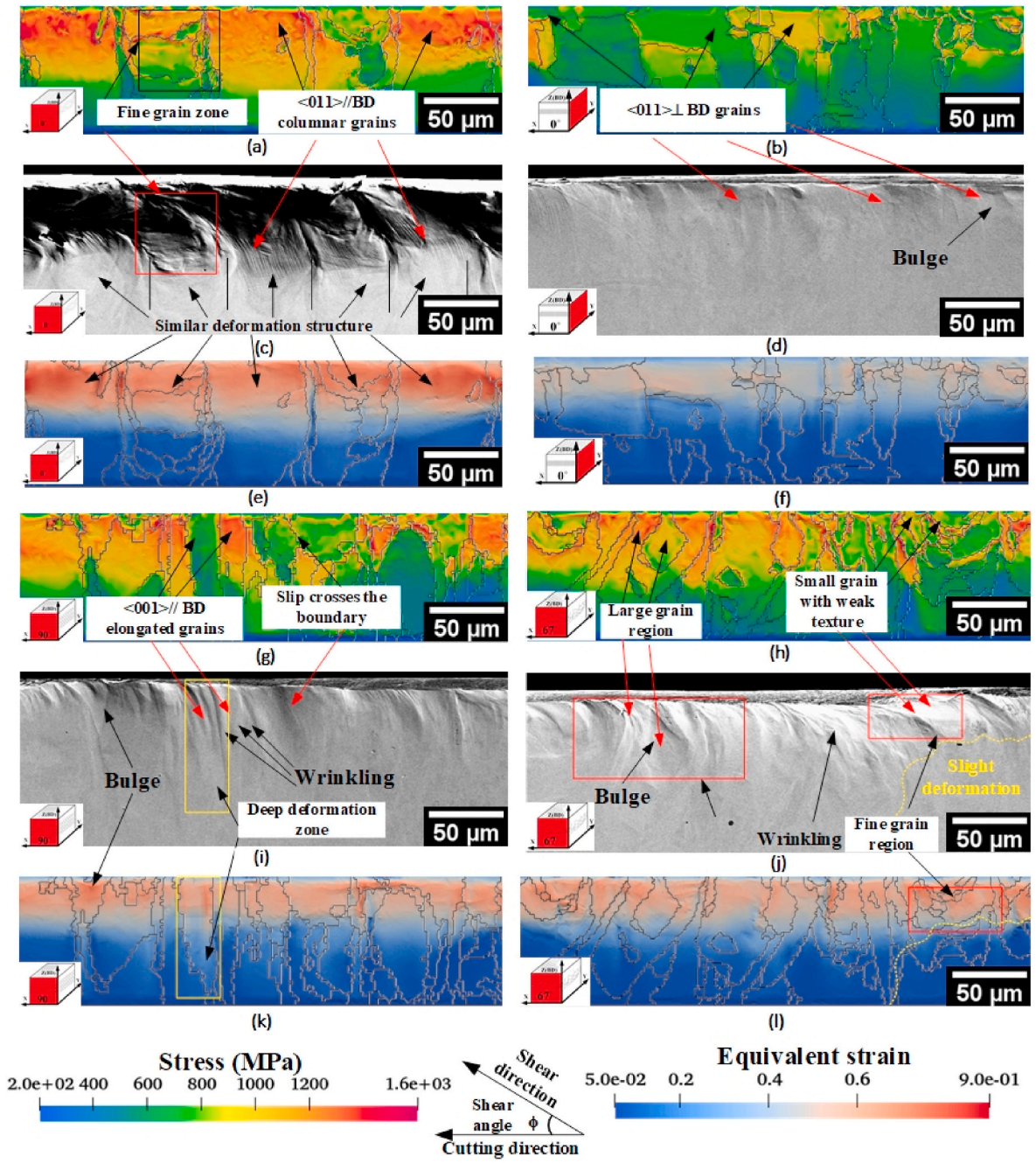

Fig. 13. Different grain-level stress and strain caused by the same shear condition. Von Mises stress of four cases for (a) 01T, (b) 02T, (g) 90T and (h) 67T; Equivalent strain in four cases for (e) 01T, (f) 02T, (k) 90T and (l) 67T. Four different deformation pattern: (c) Similar deformation structure in 01T; (d) Slightly plastic deformation in 02T; (i) Narrow and deep deformation zone in 90T due to elongated grains and (j) significant wrinkling and bulge in 67T (the two colour bars below represent the value of stress and strain respectively).

with no significant strain concentration occurring at the grain boundary between these two grains. The texture of 67T is characterized by weak texture and smaller grain size compared to the other three cases. As a result, the local stress distribution exhibits minimal variation grain by grain (Fig. 13f) and the deformation is hard to be evaluated by a preferred slip plane. It is found that small grains impede the stress transfer to the bulk material and restrict the deformation to a narrow region in proximity to the machined surface, as shown in fine grain region that is highlighted by yellow dashed line in Fig. 13h. Similarly, the strain transfer is impeded by such grain boundaries as shown in Fig. 13l, exhibiting high strain gradient between grain boundary. This is because the wide slip trace distribution (Fig. 12e for 67T) and high grain boundary intensity varies stress transfer along the cutting axis. Stress concentration near the grain boundary may result in high geometrically necessary density (GND) near the grain boundary (Fig. S4).

4. Discussion

4.1. The effect of texture on the shear-based deformation

In the 0°-rotation scanning strategy, laser scanning direction is not changed in adjacent layers. This provides a stable thermal pattern along BD and consequently results in two dominant cell growth patterns (elongated growth marked with yellow and 45° inclined growth marked

with green) as shown in Fig. 5a. At the side of the melt pool, cells incline 45° to BD to grow and almost occupy all sides of melt pools. Since FCC metals have three symmetrically equivalent <001> directions ([001], [010] and [100]), cells whose growth direction changes 90° still belong to the same grain. In this case, cells of which the growth direction changed about 90° (Fig. 5a green arrows) should be the same grain although they were divided by the side of the melt pool boundary. The two dominant cell growth patterns finally form build-directional blocks as shown in Fig. 8a and b. In addition, the columnar-to-equiaxed transition (CET) is also observed in the blocks as shown in Zone 1 of Fig. 8a, due to the thermal profile perturbations caused by complex molten flow. It is noted that only few strengthening phases and Laves phase are found in as-printed Alloy 718 [3], their effects on the deformation are limited during macro cutting process. Moreover, the micro-segregation is existed in cell structure (about 0.5 μm–3 μm), it can be ignored at the grain scale. Therefore, the analysis of shear-based deformation in this work is mainly based on texture and grain morphology (size and shape).

Grains created by < 011>//BD orientated cells occupy a large area in a block (e.g., Grain A in Fig. 8a) and have lower deformation resistance than slender elongated grains (e.g., Grain B in Fig. 8a) due to their large grain width along the cutting direction. The most active slip trace in these orientated grains is almost parallel to the shear direction as shown in Fig. 12a, resulting in significant deformation and intensive slip bands (Fig. 8d). Furthermore, stress concentration is often observed within these columnar grains due to their typical orientation, and the absence of grain boundaries below allows for stress transfer deeply from machined surface to the bulk material. In contrast, slender elongated grains at the border of blocks exhibit higher strength due to their short grain width along the cutting axis. The slip in columnar grain is hard to transfer to the narrow elongated grains. The combination of the above two grain shapes and their poor slip compatibility lead to a non-homogeneous deformation at the border of the block.

According to the Taylor-based shear model, the most active slip traces of <011>//BD texture are nearly parallel to the shear direction. In the case of 01T (Fig. 12e), the slip traces are concentrated in a narrow range due to the strong texture intensity. This concentration therefore leads to dramatic deformation (Fig. 13c) during orthogonal cutting. In contrast, for the 02T sample, the most active slip plane traces of <011>⊥BD texture (02T in Fig. 12e) are perpendicular to the shear force direction. This results in less deformation and fewer slip bands after cutting, as seen in Fig. 9f and g. The grains, of which the most active slip traces are parallel to the shear direction, are easier to deform, exhibiting high strain value as shown in Fig. 13e. Whilst the grains with the most slip plane traces perpendicular to the shear direction show low strain distribution within grains (Fig. 13f). This indicates that for the machining of components perpendicular to the building direction, the <011>⊥BD texture can reduce the bulk deformation as shown in Fig. 13d.

Considering texture formed by 0° rotation scanning strategy in the 3-dimensional space, <011>//BD and <011>⊥BD textures result from same grains but the perpendicular observation direction (e.g., XZ plane or YZ plane in Fig. 6a). The different stress status and plastic deformations in Fig. 13a–d suggest that cutting direction oriented in different directions to the crystallographic texture may lead to different stress concentrations on the same surface. In this case, the cutting direction selection is important when the functional surface finish is required. However, the cubic <001>//BD texture formed by 90° rotation scanning strategy (Fig. 6b) is not sensitive to the machining direction change due to its symmetrical characteristic along X or Y axis.

Although it is reported, in polycrystalline alloys, the plastic anisotropy at the grain scale differs the stress of grain from macro scale [43], in our work, the grains in 01T exhibits similar deformation structure (Fig. 13c) and slip bands after cutting, which matches well with calculated most active slip trace based on the macro strain Taylor model. This indicates that the grain deformation of high-intensity textured alloys still follow the macro shear strain model. It is also verified by the simulated stress status in 01T, where the stress mainly concentrates in <011>//BD columnar grains. This is because grains in a high-intensity textured workpiece have a dominant grain orientation. Such oriented grains are more likely to generate plenty of similar slip system combinations in terms of Taylor model (01T in Fig. 12e), resulting in a predictable deformation pattern as seen in Fig. 13c. When the texture intensity decreases, the slip system arrangement always changes grain by grain, resulting in a wide slip trace distribution (67T in Fig. 12e) and high anisotropy between grains [44]. Therefore, the stress is more likely to concentrate near the grain boundaries as shown in Fig. 13h and heterogeneous deformation between neighbouring grains is significant as seen in Fig. 13j.

4.2. The effect of grain morphology (size and shape) on the shear-based deformation in textured alloy 718

Since most grains are formed by one or two dominant grain growth patterns in each scanning strategy (Fig. 5) and the analysis region has similar texture as the counterpart bulk in each case (verified by Fig. 7 and S1: texture comparison before cutting), the selected grains and textures are statistically meaningful to compare different texture-based deformations in this work. Fig. 14 summarises the grain deformation map for the textured Alloy 718 in the orthogonal cutting. The representative grain is selected by the intersection points of the actual cutting line and grain boundaries (Supplementary Fig. S5). The cutting tool motion direction and corresponding flank angle, rake angle and shear angle are included. Different from the conventional nickel-based alloy [45], in which the grain is generally recognised as equiaxed (the average aspect is close to 1.0), grain morphology formed by LPBF may change dramatically in tens of microns due to the epitaxial growth perpendicular to the melt pool boundary (Fig. 5). The aspect ratios of grains ranges from 1.0 to larger than 3.0 [46]. In this case, the retained original grain morphology is the key to understanding the plastic deformation in textured Alloy 718 fabricated by LPBF at the grain scale. The grain shape in the map is represented by the equivalently normalised ellipse.

Grain distribution in the polar coordinate deformation map is decided by grain width (in cutting axis A_i (Fig. 14)) and the angle of the most active slip trace. The scattered ellipses represent individual grains along the machining surface, and the quantified slip trace directions for four textured samples from Fig. 12e are summarised in Fig. 14 (e.g., red area for 01T, black area for 02T, green area for 90T and blue area for 67T). It is found that scattered ellipses of different textured samples are mostly overlapped with the corresponding slip trace direction window calculated from Fig. 12e (i.e., the scattered red ellipses were nearly overlapped with the red shaded area). This indicates that the large-scale (hundreds of microns along the cutting direction) deformation tracing is representative to reveal the textured crystallographic deformation in LPBF-fabricated alloys.

The stress status simulation results in four samples (Fig. 13a, b, g and h) indicate that grains with high aspect ratio are more likely to transfer stress from machined surface to the bulk. It will lead to deeper deformation zones induced by machining, which is also proved by in strain distribution in Fig. 13e, f, k and l. This indicates that the deformation of grain formed via LPBF may exhibit greater sensitivity to the cutting depth compared to traditional equiaxed grains, due to their high aspect ratio. When such elongated grains are cut at different depths, the deformed depth may vary, subsequently impacting the deformation of neighbouring grains. The von Mises stress distribution is depended on grain morphologies and orientations as well as grains surrounded. However, samples with high texture intensity (e.g., those fabricated using 0° and 90° rotation strategies) are dominated by grains with typical orientations, leading to a corresponding dominance in stress distribution. High texture intensity allows grains to maintain a similar deformation pattern during orthogonal cutting, as illustrated in Fig. 13c and d. And the slip bands are more likely to cross the grain boundary when the neighbouring grain has similar orientation as shown in

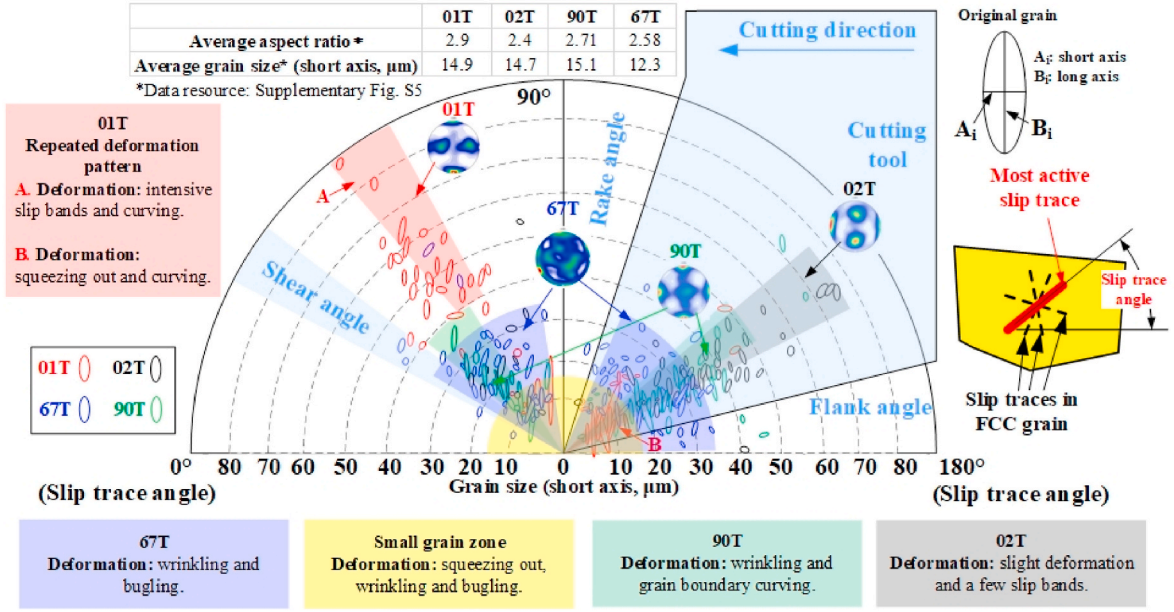

Fig. 14. Grain deformation map for textured Alloy 718 in the orthogonal cutting. Grains from 01T, 02T, 67T and 90T are represented by red, black, blue and green ellipses respectively.

Fig. 10e. In the weak texture fabricated by 67° rotation scanning strategy, the number of grains with similar orientations decreases, resulting in a variation of stress distribution from grain to grain. Consequently, slip transfer becomes more difficult to occur and the deformation pattern tends to vary locally due to variations in grain morphology and orientation. This can be observed at the large and fine grain regions in Fig. 13i.

It should be noticed that the grain deformation is decided by the orthogonal cutting process according to Eq. (A1), the shear angle and strain rate are dependent on the cutting parameters (e.g., tool rake angle and cutting speed). Corresponding to Fig. 14, the distribution of the most active slip system will change with shear-angle but the grain morphology is independent of the cutting parameters in the same cutting direction. This map enables the prediction of grain deformation for textured alloys fabricated by LPBF via grain morphologies (size and shape) and orientations in the orthogonal cutting process.

When the grain size is relatively small (e.g., <15 μm), as shown in the yellow highlighted region in Fig. 14, the grain deformation is not strongly affected by the most active trace direction because grains at this scale exhibit high deformation resistance according to the Hall-Petch effect [47]. This is because the strain gradient from machined surface to the bulk is significant, the grain deformation is dominated by width near the machined surface. On the other hand, the GND density (Fig. S4) was high in this small grain region according to Ashby's model [48]. Therefore, grains in this region are likely to be squeezed out of the free surface during plastic deformation due to plastic anisotropy. And these phenomena are indeed seen in small grain zones of all samples, such as Zone 1 in Fig. 8d and fine grains in Fig. 9f and g and 11c. The grain deformation map indicates that the activated slip trace directions of 67°-rotation scanning strategy (67T) are distributed in the range of 31°–180° and the grain size (in cutting axis A_i) is smaller than in the other three cases (average grain size is 12.1 μm). It is highly overlapped with the yellow highlighted zone (small grain zone), where wrinkling and budge are significant as seen in Fig. 13i.

In the 01T sample (XZ plane of 0° rotation scanning strategy), severe plastic deformation occurs in Zone A. These grains correspond to the <011>//BD columnar grains seen in Fig. 7. However, grains in Zone B have high deformation resistance, resulting in a significant squeezing-out effect and grain boundary curving. The combination of columnar grains and slender elongated grains fabricated by LPBF leads to similar deformation patterns. Such textured deformation only can be found by tracing the grain deformation along the cutting direction at a large scale (e.g., hundreds of microns).

The grain size and aspect ratio for the 02T sample (YZ plane of 0° rotation scanning strategy) are smaller than 01T and the slip trace direction is nearly perpendicular to the shear angle. Therefore, the grains exhibit high deformation resistance than 01T and slight grain boundary curving and few slipping are observed in this sample, as shown previously in Fig. 13d. Grains in 90T (formed by 90° rotation scanning strategy) have a similar average grain size and aspect ratio as 01T, but the grain size mainly distributes within 40 μm. Therefore, the grains in 90T do not exhibit intensive slip bands as 01T but the deformation depth is larger when the high aspect ratio grains are deformed. This is indeed seen in Fig. 13i.

This deformation map statistically summarised texture-based plastic deformation in the orthogonal cutting process by considering the original grain morphology and orientation. From this quasi-in-situ EBSD investigation, the cutting tool geometry and grain orientation are linked together in Fig. 14. However, extracting the deformation pattern from this statistically based map for an individual grain with specific size and orientation is unreliable, due to the intricate nature of grain geometry and complexity of deformation in neighbouring grains. The future machining-induced deformation theoretical model at grain scale may have to consider a deformation field that includes tens of grains with specific structures (e.g., morphologies and orientations) in front of the cutting edge to predict the possible plastic deformation.

The full-field crystal plasticity simulation results are meaningful for understanding the variations in stress status resulting from different grain structures (morphology and orientation) when an orthogonal-cutting-based loading is applied to the textured Alloy 718. However, it has to acknowledge that the actual machining process is more intricate and multifaceted than this loading condition. Therefore, the stress status evolution in the dynamic cutting process and the influence of chip formation are needed further investigation. The method used in this work, including obtaining EBSD data before cutting, full-field crystal plasticity simulation and capturing deformation pattern after cutting without polishing, can be applied to investigate machining-induced deformation in other metal materials. However, considering the limitation of EBSD detection area and sample preparation process, this method may not be suitable for large-area deformation tracing. Since this work is based on

three commonly used scanning strategies, the deformation pattern and map are helpful for additive manufacturers to adopt favourable building directions that will enable easier post-processing (e.g. cutting operations). This work emphasises the importance of characterising original microstructure (such as grain morphology and orientations) before cutting in the investigation of machining-induced deformation. This enables precise modelling of simulation based on EBSD data and direct validation via preserved plastic deformation pattern on the pre-polished surface. The grain obtained by AM cannot be easily estimated by average grain size. The grain shape should be considered, especially the grain width along the cutting direction. This is different from traditionally equiaxed grains.

5. Conclusions

This study presents a quasi-in-situ investigation of the grain deformation of LPBF-fabricated alloy before and after shear-based deformation via EBSD and SEM. Three scanning strategies, namely 0°, 90° and 67° rotation, were employed to fabricate the unique crystallographic textured LPBF structures (e.g. Alloy 718). It is the first time that shear-based textured deformation can be traced grain by grain along the cutting direction for hundreds of microns before and after cutting. The grain response to the shear deformation in different crystallographic textured LPBF-fabricated samples was quantified in the deformation map. The main conclusions are drawn below:

- In crystallographically textured materials fabricated by LPBF, the shear based deformation (e.g. cutting) was strongly affected by preferred slip system and unique grain morphologies. In our case study three totally different textures (<011>//BD, <011>⊥BD and <001>//BD) have been obtained by changing the scanning strategies. A similar deformation structure is observed in 0° rotation scanning strategy fabricated sample (01T) when cutting direction is perpendicular to the laser scanning direction. This is because stress concentration is more likely to occur in the columnar grain with high intensity <011>//BD texture. However, the stress concentration is reduced in <011>⊥BD texture, resulting in slightly plastic deformation. The deformation in weak texture region varies locally due to the variable grain morphologies and the absence of a dominant stress distribution from preferred orientation of grains.
- Unidirectional (i.e. 0° rotation scanning strategy) LPBF built structures characterised by very heterogeneous crystallographic textures will lead to dramatically different strain/stress levels in two cutting directions. This is because the three-dimensional grain growth pattern (side-branching) in LPBF enables the same grain to exhibit non-equivalent textures (<011>//BD and <011>⊥BD) on XZ and YZ planes. Consequently, different activated slip systems in cutting process lead to dramatic deformation in <011>//BD texture but slight deformation in <011>⊥BD texture. For the XY surface machining, the cubic <001>//BD texture and weak texture fabricated by 90°, 67° rotation strategies are symmetrical equivalent in both XZ and YZ planes. It will not cause deformation deviation when cutting direction changes 90°.
- Statistical deformation tendency map not only exhibits the relationship between texture/slip system and shear angle but also revealed the threshold of grain size that affects the texture-based deformation. Individual grain deformation in a textured alloy 718 is strongly depends on its grain width along the cutting direction. In the large grain (large grain width along the cutting direction) region, the grain with a small activated slip trace angle (parallel to the shear direction) is easy to deform. But slight deformation occurs to the grain when the activated slip trace angle is large. Small grains width exhibit high deformation resistance due to the high geometrically necessary dislocation (GND), hindering the plastic deformation along the slip direction.

From generic point of view, our study provides a route to evaluate the how the grain shapes with high aspect ratios existent in crystallographically textured structures affect their deformation levels in machining. This is of relevance to many shear removal processes that routinely are employed after the LPBF process. In addition, this work raises awareness of the importance of capturing the microstructure details (e.g. crystallographic orientation) at grain level before and after cutting so that the influence of cutting on deformation of single/multiple grains can be understood; this will also provide key information for detailed modelling of cutting when considering microstructure at grain level.

CRediT authorship contribution statement

Lingshan Li: Writing – original draft, Methodology, Investigation, Formal analysis, Data curation. **Hao Chen:** Writing – review & editing, Supervision, Methodology, Investigation. **Zhirong Liao:** Writing – review & editing, Supervision, Methodology, Investigation, Conceptualization. **Yue Yang:** Methodology, Investigation, Data curation. **Dragos Axinte:** Writing – review & editing, Supervision, Methodology, Investigation, Conceptualization.

Declaration of competing interest

The authors declare that they have no known competing financial interests or personal relationships that could have appeared to influence the work reported in this paper.

Data availability

Data will be made available on request.

Acknowledgments

This research was supported by Zhejiang Natural Science Programme under Grant No. LY22E010004, Natural Science Foundation of China under Grant No. 51901107 and National Key Lab Fund under Grant No. JCKY61420052013.

Appendix A

The shear strain ε in the shear plane is estimated based on [49]:

$$\varepsilon = \frac{\cos \gamma_n}{2\sqrt{3} sin\ \varphi_n \cos(\varphi_n - \gamma_n)} \tag{A1}$$

where γ_n is the rake angle and φ_n is the shear angle, which was estimated by the Merchant theory [33]. The angle calculated by analytical method is decided by the cutting tool geometry and cutting direction mentioned in Section 2.3. The plane-strain transformed from the shear plane (SP) into the sample frame (Fig. 4) via transformation matrixes in Eq. (A2):

$$g^{\text{shear}\rightarrow\text{sample}} = \begin{pmatrix} \cos\varphi & -\sin\varphi & 0 \\ \sin\varphi & \cos\varphi & 0 \\ 0 & 0 & 1 \end{pmatrix} \tag{A2}$$

The shear strain loaded in the sample frame is calculated by Eq. (A3):

$$\in_{ij}^{sample} = g_{ik}^{shear\rightarrow sample} g_{jl}^{shear\rightarrow sample} g_{kl}^{shear} = \frac{d\varepsilon}{2} \begin{pmatrix} -\sin 2\varphi & \cos 2\varphi & 0 \\ \cos 2\varphi & \sin 2\varphi & 0 \\ 0 & 0 & 0 \end{pmatrix} \tag{A3}$$

where $g_{ik}^{shear\rightarrow sample}$ is the transformation matrix used to rotate the deformation gradient of Eq. (1) to the sample frame. The transformation from the sample frame to the crystal frame is via Eqs. (A4) and (A5):

$$g^{\text{sample}\rightarrow\text{crystal}} = \begin{pmatrix} u & o & h \\ v & p & k \\ w & q & l \end{pmatrix} \tag{A4}$$

$$\in_{ij}^{crystal} = g_{ik}^{sample\rightarrow crystal} g_{jl}^{sample\rightarrow crystal} g_{kl}^{sample} \tag{A5}$$

where [uvw] and (hkl) represent the cutting direction and the cutting plane, respectively. The coordinate transformation matrix $g^{\text{sample}\rightarrow\text{crystal}}$ is dependent on both the current sample frame and orientated crystal coordinates [50]. The shear strain then can be applied to each grain to calculate the most active slip direction. It should be noted that the final shear strain in each crystal frame is different for the different oriented crystal frames.

Appendix B

Slip trace calculation.

All slip system:

u	v	w	h	k	l
0	−1	−1	−1	1	−1
−1	−1	0	−1	1	−1
1	0	−1	−1	1	−1
0	−1	1	−1	−1	−1
1	−1	0	−1	−1	−1
1	0	−1	−1	−1	−1
0	−1	1	1	−1	−1
−1	0	−1	1	−1	−1
−1	−1	0	1	−1	−1
0	−1	−1	1	1	−1
1	−1	0	1	1	−1
−1	0	−1	1	1	−1

(B1)

In this minimum energy deformation system [51], We assume the shear deformation is based on the minimum energy theory. For a grain with an orientation, there is an angle (θ) between the shear direction (s) and slip system (Eq. (B1), slip plane normal, **n** (h, k, l), and slip direction, **d** (u, v, w)). Since the burgers vector (b) is parallel to the slip direction (in general) and this model assumes that all slip directions have the same critical resolved shear stress, the strain in the crystal frame can be normalised and calculated along each slip direction.

Since the strain is symmetric and only 5 slip system need to be calculated by Eq. (3), the minimum W was obtained by the sum of critical resolved shear stress. The most active slip direction has the maximum displacement component along the slip direction and the corresponding slip plane is the most active. The most active slip system is given by:

$$b^{\alpha} = Max\left|b^{i}(\delta w)\right| \tag{B2}$$

The relevant slip plane (most active slip plane) is:

$$n^{\alpha} = \left|\left(b_{Max}^{\alpha}\right)\right| \tag{B3}$$

Since the most active slip planes of oriented grains are calculated in individual crystal frames, they should be transformed from the crystal frame to the sample frame based on Eqs. (A3) and (A4). After the frame transformation, the most active slip trace t_m is defined as the intersecting line of the most active slip plane and the sample plane, XY plane (Plane_{xy}) in Fig. 4:

$$t_m = n^{\alpha} \cap \text{Plane}_{xy} \tag{B4}$$

Considering the Euler angle of each pixel in the EBSD, we calculated the most active slip direction from 12 slip systems (24 slip directions if considering opposite direction) and put it in a spherical coordinate, shown as Fig. 12 (partly similar to the PF). Since the Euler angle within a grain may be similar, the calculation step can be set as 5 μm to save computing time. The intensity is the weight of a slip trace in all slip traces. The grain size is considered because large grains (more pixels) have high weight than small grains.

Appendix C

The PRISMS-Plasticity, an open-source software was employed here to simulate full-field crystal plasticity [35]. The evolution of slip resistance for slip system α can be calculated by:

$$\dot{s}^{\alpha} = \sum_{\beta} h^{\alpha\beta}\dot{\gamma}^{\beta} \tag{C1}$$

where $h^{\alpha\beta}$ is hardening moduli, which defines the variation of slip resistance for slip system α due to the slip rate on slip system β. The hardening moduli $h^{\alpha\beta}$ is considering the combined effect of work hardening and recovery as follows:

$$h^{\alpha\beta} = q^{\alpha\beta}h_o\left(1 - \frac{s^{\beta}}{s_s}\right)^{m} \tag{C2}$$

where $q^{\alpha\beta}$ is the latent hardening ratio, h_o donates the hardening parameter for slip system β, s^{β} is the slip resistance at hardening saturation, s_s is the saturation stress where large plastic flow initiates and m is a material constant that governs the sensitivity of the hardening moduli to the slip resistance. The crystal plasticity model is detailed in Ref. [52] and the material constants for the simulation are obtained from Ref. [53]. The material constants used in the four cases are identical because the fabrication parameters are also the same. Therefore, the simulation only varies in terms of grain morphology and orientation.

To mesh the EBSD data for plasticity simulation, a 400 × 90 μm region was directly processed using Gmsh [54] as illustrated in Fig. S6. As the EBSD results were obtained prior to the cutting process, the preserved grain morphologies were carefully retained to prevent errors arising from distortions near the machined surface. This approach could enhance the simulation accuracy since the loading is applied to the original grains. To fix the bulk material, a nodal boundary condition was employed, while a loading condition, obtained from the analytical model of Eq. (A1), was applied to the region near the machined surface. The total simulation time was set as 1e-5s to reach a high strain rate whilst the time increment was 1e-9s for simulation convergence. The post-processing was finished by ParaView, an open-source software for visualization.

Appendix D. Supplementary data

Supplementary data to this article can be found online at https://doi.org/10.1016/j.ijmachtools.2023.104050.

References

[1] F. Caiazzo, V. Alfieri, G. Corrado, P. Argenio, Laser powder-bed fusion of Inconel 718 to manufacture turbine blades, Int. J. Adv. Manuf. Technol. 93 (2017) 4023–4031, https://doi.org/10.1007/s00170-017-0839-3.

[2] D. Gu, X. Shi, R. Poprawe, D.L. Bourell, R. Setchi, J. Zhu, Material-structure-performance integrated laser-metal additive manufacturing, Science (80) (2021) 372, https://doi.org/10.1126/science.abg1487, eabg1487.

[3] P. Tao, H. Li, B. Huang, Q. Hu, S. Gong, Q. Xu, The crystal growth, intercellular spacing and microsegregation of selective laser melted Inconel 718 superalloy, Vacuum 159 (2019) 382–390, https://doi.org/10.1016/j.vacuum.2018.10.074.

[4] H. Yeung, F.H. Kim, M.A. Donmez, J. Neira, Keyhole pores reduction in laser powder bed fusion additive manufacturing of nickel alloy 625, Int. J. Mach. Tool Manufact. 183 (2022), 103957, https://doi.org/10.1016/J.IJMACHTOOLS.2022.103957.

[5] X.X. Zhang, A. Lutz, H. Andrä, M. Lahres, W.M. Gan, E. Maawad, C. Emmelmann, Evolution of microscopic strains, stresses, and dislocation density during in-situ tensile loading of additively manufactured AlSi10Mg alloy, Int. J. Plast. 139 (2021), 102946, https://doi.org/10.1016/J.IJPLAS.2021.102946.

[6] K. Karami, A. Blok, L. Weber, S.M. Ahmadi, R. Petrov, K. Nikolic, E.V. Borisov, S. Leeflang, C. Ayas, A.A. Zadpoor, M. Mehdipour, E. Reinton, V.A. Popovich, Continuous and pulsed selective laser melting of Ti6Al4V lattice structures: effect of post-processing on microstructural anisotropy and fatigue behaviour, Addit. Manuf. 36 (2020), 101433, https://doi.org/10.1016/j.addma.2020.101433.

[7] P. Van Cauwenbergh, V. Samaee, L. Thijs, J. Nejezchlebová, P. Sedlák, A. Iveković, D. Schryvers, B. Van Hooreweder, K. Vanmeensel, Unravelling the multi-scale structure–property relationship of laser powder bed fusion processed and heat-treated AlSi10Mg, Sci. Rep. 11 (2021) 6423, https://doi.org/10.1038/s41598-021-85047-2.

[8] D. Zhang, H. Li, X. Guo, Y. Yang, X. Yang, Z. Feng, An insight into size effect on fracture behavior of Inconel 718 cross-scaled foils, Int. J. Plast. 153 (2022), 103274, https://doi.org/10.1016/J.IJPLAS.2022.103274.

[9] A. Malakizadi, D. Mallipeddi, S. Dadbakhsh, R. M'Saoubi, P. Krajnik, Post-processing of additively manufactured metallic alloys – a review, Int. J. Mach. Tool Manufact. 179 (2022), 103908, https://doi.org/10.1016/J.IJMACHTOOLS.2022.103908.

[10] H. Jia, H. Sun, H. Wang, Y. Wu, H. Wang, Scanning strategy in selective laser melting (SLM): a review, Int. J. Adv. Manuf. Technol. 113 (2021) 2413–2435, https://doi.org/10.1007/s00170-021-06810-3.

[11] A. Keshavarzkermani, R. Esmaeilizadeh, U. Ali, P.D. Enrique, Y. Mahmoodkhani, N.Y. Zhou, A. Bonakdar, E. Toyserkani, Controlling mechanical properties of additively manufactured hastelloy X by altering solidification pattern during laser powder-bed fusion, Mater. Sci. Eng. 762 (2019), 138081, https://doi.org/10.1016/J.MSEA.2019.138081.

[12] E. Hosseini, V.A. Popovich, A review of mechanical properties of additively manufactured Inconel 718, Addit. Manuf. 30 (2019), 100877, https://doi.org/10.1016/j.addma.2019.100877.

[13] M. Zheng, L. Wei, J. Chen, Q. Zhang, G. Zhang, X. Lin, W. Huang, On the role of energy input in the surface morphology and microstructure during selective laser melting of Inconel 718 alloy, J. Mater. Res. Technol. 11 (2021) 392–403, https://doi.org/10.1016/j.jmrt.2021.01.024.

[14] A. Rezaei, A. Rezaeian, A. Kermanpur, M. Badrossamay, E. Foroozmehr, M. Marashi, A. Foroozmehr, J. Han, Microstructural and mechanical anisotropy of selective laser melted IN718 superalloy at room and high temperatures using small punch test, Mater. Char. 162 (2020), 110200, https://doi.org/10.1016/j.matchar.2020.110200.

[15] S.H. Sun, K. Hagihara, T. Nakano, Effect of scanning strategy on texture formation in Ni-25 at.%Mo alloys fabricated by selective laser melting, Mater. Des. 140 (2018) 307–316, https://doi.org/10.1016/J.MATDES.2017.11.060.

[16] X. Wang, J. Kang, T. Wang, P. Wu, T. Feng, L. Zheng, Effect of layer-wise varying parameters on the microstructure and soundness of selective laser melted INCONEL 718 alloy, Materials 12 (2019), https://doi.org/10.3390/ma12132165.

[17] X. Zhang, H. Xu, Z. Li, A. Dong, D. Du, L. Lei, G. Zhang, D. Wang, G. Zhu, B. Sun, Effect of the scanning strategy on microstructure and mechanical anisotropy of Hastelloy X superalloy produced by Laser Powder Bed Fusion, Mater. Char. 173 (2021), 110951, https://doi.org/10.1016/j.matchar.2021.110951.

[18] G.E. Bean, T.D. McLouth, D.B. Witkin, S.D. Sitzman, P.M. Adams, R.J. Zaldivar, Build orientation effects on texture and mechanical properties of selective laser melting Inconel 718, J. Mater. Eng. Perform. 28 (2019) 1942–1949, https://doi.org/10.1007/s11665-019-03980-w.

[19] S. Periane, A. Duchosal, S. Vaudreuil, H. Chibane, A. Morandeau, J. Cormier, R. Leroy, Machining influence on the fatigue resistance of Inconel 718 fabricated by selective laser melting (SLM), in: Procedia Struct. Integr., Elsevier B.V., 2019, pp. 415–422, https://doi.org/10.1016/j.prostr.2019.12.045.

[20] A. la Monaca, J.W. Murray, Z. Liao, A. Speidel, J.A. Robles-Linares, D.A. Axinte, M. C. Hardy, A.T. Clare, Surface integrity in metal machining - Part II: functional performance, Int. J. Mach. Tool Manufact. 164 (2021), 103718, https://doi.org/10.1016/J.IJMACHTOOLS.2021.103718.

[21] E. Abbá, A. Speidel, Z. Liao, D. Axinte, D. Novovic, A bar of cutting fluid: deep Eutectic Fluids with a novel flavour, Mater. Today Adv. 16 (2022), 100291, https://doi.org/10.1016/J.MTADV.2022.100291.

[22] Z. Zhao, L. Li, W. Yang, Y. Zeng, Y. Lian, Z. Yue, A comprehensive study of the anisotropic tensile properties of laser additive manufactured Ni-based superalloy after heat treatment, Int. J. Plast. 148 (2022), 103147, https://doi.org/10.1016/J.IJPLAS.2021.103147.

[23] S. Ghorbanpour, M.E. Alam, N.C. Ferreri, A. Kumar, B.A. McWilliams, S.C. Vogel, J. Bicknell, I.J. Beyerlein, M. Knezevic, Experimental characterization and crystal plasticity modeling of anisotropy, tension-compression asymmetry, and texture evolution of additively manufactured Inconel 718 at room and elevated temperatures, Int. J. Plast. 125 (2020) 63–79, https://doi.org/10.1016/J.IJPLAS.2019.09.002.

[24] A. Malakizadi, T. Hajali, F. Schulz, S. Cedergren, J. Ålgårdh, R. M'Saoubi, E. Hryha, P. Krajnik, The role of microstructural characteristics of additively manufactured Alloy 718 on tool wear in machining, Int. J. Mach. Tool Manufact. 171 (2021), 103814, https://doi.org/10.1016/J.IJMACHTOOLS.2021.103814.

[25] Z. Liao, A. la Monaca, J. Murray, A. Speidel, D. Ushmaev, A. Clare, D. Axinte, R. M'Saoubi, Surface integrity in metal machining - Part I: fundamentals of surface characteristics and formation mechanisms, Int. J. Mach. Tool Manufact. 162 (2021), 103687, https://doi.org/10.1016/J.IJMACHTOOLS.2020.103687.

[26] Z. Wang, J. Zhang, Z. Xu, J. Zhang, G. Li, H. Zhang, Z. Li, H. ul Hassan, F. Fang, A. Hartmaier, Y. Yan, T. Sun, Crystal anisotropy-dependent shear angle variation in orthogonal cutting of single crystalline copper, Precis. Eng. 63 (2020) 41–48, https://doi.org/10.1016/j.precisioneng.2020.01.006.

[27] D. Xu, T.E.J. Edwards, Z. Liao, X. Maeder, R. Ramachandramoorthy, M. Jain, J. Michler, D. Axinte, Revealing Nanoscale deformation mechanisms caused by shear-based material removal on individual grains of a Ni-based superalloy, Acta Mater. 212 (2021), 116929, https://doi.org/10.1016/j.actamat.2021.116929.
[28] D. Axinte, H. Huang, J. Yan, Z. Liao, What micro-mechanical testing can reveal about machining processes, Int. J. Mach. Tool Manufact. 183 (2022), 103964, https://doi.org/10.1016/j.ijmachtools.2022.103964.
[29] E. Tekoğlu, A.D. O'Brien, J. Liu, B. Wang, S. Kavak, Y. Zhang, S.Y. Kim, S. Wang, D. Ağaoğulları, W. Chen, A.J. Hart, J. Li, Strengthening additively manufactured Inconel 718 through in-situ formation of nanocarbides and silicides, Addit. Manuf. 67 (2023), 103478, https://doi.org/10.1016/J.ADDMA.2023.103478.
[30] D. Xu, Z. Liao, D. Axinte, M. Hardy, A novel method to continuously map the surface integrity and cutting mechanism transition in various cutting conditions, Int. J. Mach. Tool Manufact. 151 (2020), 103529, https://doi.org/10.1016/j.ijmachtools.2020.103529.
[31] F. Bachmann, R. Hielscher, H. Schaeben, Texture analysis with MTEX – free and open source software toolbox, Solid State Phenom. 160 (2010) 63–68, https://doi.org/10.4028/www.scientific.net/SSP.160.63.
[32] E. Demir, A Taylor-based plasticity model for orthogonal machining of single-crystal FCC materials including frictional effects, Int. J. Adv. Manuf. Technol. 40 (2009) 847–856, https://doi.org/10.1007/s00170-008-1409-5.
[33] W. Grzesik, Orthogonal and oblique cutting mechanics, in: Adv. Mach. Process. Met. Mater., Elsevier, 2017, pp. 93–111, https://doi.org/10.1016/B978-0-444-63711-6.00006-5.
[34] K.S. Woon, M. Rahman, F.Z. Fang, K.S. Neo, K. Liu, Investigations of tool edge radius effect in micromachining: a FEM simulation approach, J. Mater. Process. Technol. 195 (2008) 204–211, https://doi.org/10.1016/j.jmatprotec.2007.04.137.
[35] M. Yaghoobi, S. Ganesan, S. Sundar, A. Lakshmanan, S. Rudraraju, J.E. Allison, V. Sundararaghavan, PRISMS-plasticity: an open-source crystal plasticity finite element software, Comput. Mater. Sci. 169 (2019), 109078, https://doi.org/10.1016/J.COMMATSCI.2019.109078.
[36] M.-S. Pham, B. Dovgyy, P.A. Hooper, C.M. Gourlay, A. Piglione, The role of side-branching in microstructure development in laser powder-bed fusion, Nat. Commun. 11 (2020) 749, https://doi.org/10.1038/s41467-020-14453-3.
[37] O. Andreau, I. Koutiri, P. Peyre, J.D. Penot, N. Saintier, E. Pessard, T. De Terris, C. Dupuy, T. Baudin, Texture control of 316L parts by modulation of the melt pool morphology in selective laser melting, J. Mater. Process. Technol. 264 (2019) 21–31, https://doi.org/10.1016/J.JMATPROTEC.2018.08.049.
[38] J.J. Marattukalam, D. Karlsson, V. Pacheco, P. Beran, U. Wiklund, U. Jansson, B. Hjörvarsson, M. Sahlberg, The effect of laser scanning strategies on texture, mechanical properties, and site-specific grain orientation in selective laser melted 316L SS, Mater. Des. 193 (2020), 108852, https://doi.org/10.1016/J.MATDES.2020.108852.
[39] H. Ghadbeigi, S.R. Bradbury, C. Pinna, J.R. Yates, Determination of micro-scale plastic strain caused by orthogonal cutting, Int. J. Mach. Tool Manufact. 48 (2008) 228–235, https://doi.org/10.1016/j.ijmachtools.2007.08.017.
[40] L.L. Li, Z.J. Zhang, P. Zhang, J.B. Yang, Z.F. Zhang, Distinct fatigue cracking modes of grain boundaries with coplanar slip systems, Acta Mater. 120 (2016) 120–129, https://doi.org/10.1016/J.ACTAMAT.2016.06.032.
[41] T.R. Bieler, R. Alizadeh, M. Peña-Ortega, J. Llorca, An analysis of (the lack of) slip transfer between near-cube oriented grains in pure Al, Int. J. Plast. 118 (2019) 269–290, https://doi.org/10.1016/j.ijplas.2019.02.014.
[42] E. Soufian, R. Darabi, M. Abouridouane, A. Reis, T. Bergs, Numerical predictions of orthogonal cutting–induced residual stress of super alloy Inconel 718 considering dynamic recrystallization, Int. J. Adv. Manuf. Technol. 122 (2022) 601–617, https://doi.org/10.1007/S00170-022-09846-1/FIGURES/19.
[43] M.P. Petkov, E. Elmukashfi, E. Tarleton, A.C.F. Cocks, Evaluation of local stress state due to grain-boundary sliding during creep within a crystal plasticity finite element multi-scale framework, Int. J. Mech. Sci. 211 (2021), 106715, https://doi.org/10.1016/J.IJMECSCI.2021.106715.
[44] H.M. Zbib, T. Diaz de la Rubia, A multiscale model of plasticity, Int. J. Plast. 18 (2002) 1133–1163, https://doi.org/10.1016/S0749-6419(01)00044-4.
[45] A. la Monaca, D.A. Axinte, Z. Liao, R. M'Saoubi, M.C. Hardy, Towards understanding the thermal history of microstructural surface deformation when cutting a next generation powder metallurgy nickel-base superalloy, Int. J. Mach. Tool Manufact. 168 (2021), 103765, https://doi.org/10.1016/j.ijmachtools.2021.103765.
[46] E. Paccou, M. Mokhtari, C. Keller, J. Nguejio, W. Lefebvre, X. Sauvage, S. Boileau, P. Babillot, P. Bernard, E. Bauster, Investigations of powder reusing on microstructure and mechanical properties of Inconel 718 obtained by additive manufacturing, Mater. Sci. Eng. 828 (2021), 142113, https://doi.org/10.1016/J.MSEA.2021.142113.
[47] L. Jiang, H. Fu, H. Zhang, J. Xie, Physical mechanism interpretation of polycrystalline metals' yield strength via a data-driven method: a novel Hall–Petch relationship, Acta Mater. 231 (2022), 117868, https://doi.org/10.1016/J.ACTAMAT.2022.117868.
[48] M.F. Ashby, The deformation of plastically non-homogeneous materials, Philos. Mag. A 21 (1970) 399–424, https://doi.org/10.1080/14786437008238426.
[49] P.L.B. Oxley, M.C. Shaw, Mechanics of machining: an analytical approach to assessing machinability, J. Appl. Mech. 57 (1990) 253, https://doi.org/10.1115/1.2888318.
[50] E. Demir, C. Mercan, A physics-based single crystal plasticity model for crystal orientation and length scale dependence of machining response, Int. J. Mach. Tool Manufact. 134 (2018) 25–41, https://doi.org/10.1016/J.IJMACHTOOLS.2018.06.004.
[51] H.J. Bunge, Some applications of the Taylor theory of polycrystal plasticity, Krist. Tech. 5 (1970) 145–175, https://doi.org/10.1002/crat.19700050112.
[52] K.S. Stopka, M. Yaghoobi, J.E. Allison, D.L. McDowell, Simulated effects of sample size and grain neighborhood on the modeling of extreme value fatigue response, Acta Mater. 224 (2022), 117524, https://doi.org/10.1016/J.ACTAMAT.2021.117524.
[53] P. Fernandez-Zelaia, Y. Lee, S. Dryepondt, M.M. Kirka, Creep anisotropy modeling and uncertainty quantification of an additively manufactured Ni-based superalloy, Int. J. Plast. 151 (2022), 103177, https://doi.org/10.1016/J.IJPLAS.2021.103177.
[54] D. Depriester, R. Kubler, MTEX2Gmsh: a tool for generating 2D meshes from EBSD data, J. Open Source Softw. 5 (2020) 2094, https://doi.org/10.21105/JOSS.02094.